Status update on the US ODS development program

Nuclear Technology Research and Development

Prepared for
GenIV SFR-AF PMB
Stuart Maloy
Los Alamos National Laboratory
2016

SUMMARY

Three papers are attached highlighting some recent progress in the development and testing of Oxide Dispersion Strengthened ferritic steels in tube and plate form. Aydogan et al. (2016) and Alam et al. (2016) papers summarize testing and characterization that has been performed on plate and tube materials. In the Alam et al. paper it was noted that after cross-rolling plate material of 14YWT, microcracks were formed. This resulted from an (001) texture in the plane normal to the plate causing cracking microcracking within that plane. Such microcracking affects low temperature tensile properties up to 200C. It was not seen in tube material produced by hydrostatic extrusion. In the Aydogan et al. (2016) paper characterization was performed on tubes produced from the ODS material, 14YWT. Tubes were formed through hydrostatic extrusion of plate material and hydrostatic extrusion of spray formed tubes. It was noted that strong texture on {001}<110> was formed in the plate material while shear deformation during hot extrusion produced a strong <111> ll ND texture component. In the Aydogan et al. (2017) paper detailed analysis was performed on the change in oxide size with ion irradiation to doses >500 dpa at 450C. The results show strong stability for the 2-4 nm oxide particles with a reduction in size ~25% after 270 dpa and an increase in density.

Materials Science & Engineering A 675 (2016) 437–448

Contents lists available at ScienceDirect

Materials Science & Engineering A

journal homepage: www.elsevier.com/locate/msea

Tensile deformation and fracture properties of a 14YWT nanostructured ferritic alloy

M.E. Alam [a,*], S. Pal [a], K. Fields [a], S.A. Maloy [b], D.T. Hoelzer [c], G.R. Odette [a]

[a] Materials Department, University of California, Santa Barbara, CA 93106, USA
[b] Los Alamos National Laboratory, Los Alamos, NM 87545, USA
[c] Materials Science and Technology Division, Oak Ridge National Laboratory, Oak Ridge, TN 37830, USA

ARTICLE INFO

Article history:
Received 6 May 2016
Received in revised form
27 May 2016
Accepted 12 August 2016
Available online 13 August 2016

Keywords:
Nanostructured ferritic alloy
Nano oxide
Delamination
Tensile properties
Fractography

ABSTRACT

A new larger heat of a 14YWT nanostructured ferritic alloy (NFA), FCRD NFA-1, was synthesized by ball milling FeO and argon atomized Fe-14Cr-3W-0.4Ti-0.2Y (wt%) powders, followed by hot extrusion, annealing and cross rolling to produce an ≈10 mm-thick plate. NFA-1 contains a bimodal size distribution of pancake-shaped, mostly very fine scale, grains. The as-processed plate also contains a large population of microcracks running parallel to its broad surfaces. The small grains and large concentration of Y–Ti–O nano-oxides (NOs) result in high strength up to 800 °C. The uniform and total elongations range from ≈1–8%, and ≈10–24%, respectively. The strength decreases more rapidly above ≈400 °C and deformation transitions to largely viscoplastic creep by ≈600 °C. While the local fracture mechanism is generally ductile-dimple microvoid nucleation, growth and coalescence, perhaps the most notable feature of tensile deformation behavior of NFA-1 is the occurrence of periodic delamination, manifested as fissures on the fracture surfaces.

1. Introduction

The success of advanced nuclear fission and future fusion energy sources depends on the development of new, high performance structural materials that can sustain extended component lifetimes in extremely hostile irradiation environments. Nanostructured ferritic alloys (NFAs), which are leading candidates for these applications, have high tensile, fatigue and creep strengths over a wide range of temperatures, as well as outstanding irradiation tolerance and unique thermal stability up to 900 °C [1–3]. The outstanding properties of 12–14%Cr NFAs are derived from the presence of submicron (~500 nm) grains, high dislocation densities ($0.5-2\times10^{15}/m^2$) and an ultrahigh population ($10^{23}-10^{24}/m^3$) of nanometer scale (2–4 nm) Y–Ti–O rich multifunctional nano-oxides (NOs). The NOs retard dislocation climb and glide, stabilize grain and dislocation structures, and trap helium in fine bubbles that retard swelling and grain boundary embrittlement [1–7]. Unlike some high strength materials, NFAs often exhibit significant ductility and in some cases reasonable fracture toughness in standard test orientations [8–12].

NFAs are typically described by a number designating their Cr content followed by YWT indicating their primary micro-alloying elements, Y, W and Ti. A new 14YWT NFA, named FCRD NFA-1, with a nominal composition of Fe-14Cr-3W-0.4Ti-0.2Y (wt%), was developed in a collaboration between the University of California, Santa Barbara (UCSB), Los Alamos National Laboratory (LANL) and Oak Ridge National Laboratory (ORNL). The objective was to achieve a good combination of strength, ductility, toughness and irradiation tolerance in a larger heat of NFA. Processing NFA-1 involved an alternative path that involved including Y in the melt prior to gas atomization and rapid solidification. Many small lab heats of precursor NFA, with different processing and compositional variants, were first explored to identify the best practice path [3,10,13–16]. This culminated in the final production of an extruded and cross-rolled heat known as 14YWT-PM2 (PM2) [17]. NFA-1 is larger-scale heat (55 kg), processed by the same route as PM2, in the form of an ≈10mm thick plate [18].

Characterization of NOs, dislocations and grain structures of the NFA-1 are described elsewhere [18]. Here we focus on the basic tensile deformation and fracture properties of NFA-1. Companion studies of fracture toughness, texturing and the underlying micromechanism of deformation and fracture are reported elsewhere [19,20]. Unlike most previous results, a special effort is made here to characterize the effects of orientation of the test specimens with respect to the plate geometry and primary deformation processing directions. Further, the combined effect of prior plate microcracking and subsequent delamination during testing, are systematically explored for the first time. Tensile tests were carried

* Corresponding author.
E-mail address: alam@engineering.ucsb.edu (M.E. Alam).

http://dx.doi.org/10.1016/j.msea.2016.08.051
0921-5093/

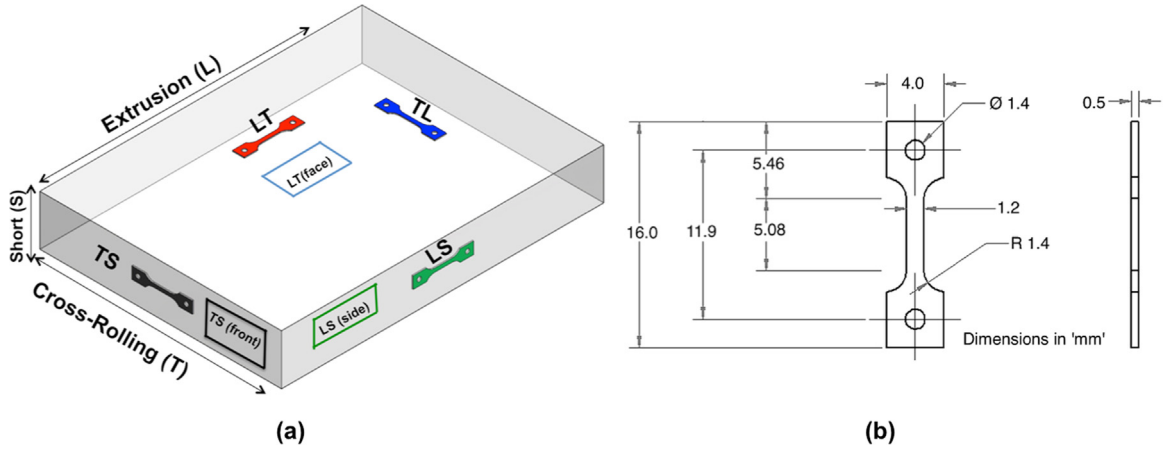

Fig. 1. (a) NFA-1 plate section views and tensile specimen orientations with respect to the extrusion, cross rolling and thickness directions; and, (b) the dimensions of the SSJ-2 dogbone tensile specimen.

Table 1
Grain morphology and microhardness of FCRD NFA-1 for the different plate sections.

Planes	Long, l (μm)	Short, s (μm)	Av, d=(l+s)/2 (μm)	Aspect ratio	Microhardness, H_v, (kg/mm^2)
LT (Face)	0.767 ± 0.566	0.517 ± 0.355	0.642 ± 0.450	1.5 ± 0.4	376 ± 18
LS (Side)	0.792 ± 0.638	0.301 ± 0.108	0.546 ± 0.343	2.7 ± 1.6	368 ± 25
TS (Front)	0.799 ± 0.833	0.296 ± 0.180	0.548 ± 0.482	2.7 ± 1.3	352 ± 39

Table 2
The average size, grain aspect ratio, number and area fractions of grains for different section views of the NFA-1 plate.

Planes	Range (μm)	Length, l (μm)	Aspect ratio, r	No. freq. of grains, (%)	Area fraction, (%)
LT (Face)	0–1	0.57 ± 0.20	1.5 ± 0.4	80	60
	1–10	1.57 ± 0.80	1.6 ± 0.4	20	40
	10+	–	–	–	–
LS (Side)	0–1	0.60 ± 0.19	2.2 ± 0.7	79.3	64.6
	1–10	1.42 ± 0.50	4.5 ± 2.0	20.5	33.2
	10+	11.3	15.8	0.2	2.2
TS (Front)	0–1	0.56 ± 0.22	2.2 ± 0.9	79.3	59.5
	1–10	1.59 ± 0.94	4.1 ± 1.5	20.5	37.9
	10+	12.94	10.0	0.2	2.6

out in air from room temperature to 800 °C. Scanning electron microscopy (SEM) was used to examine grain size, coarser oxide features, microcracks, fracture surfaces, and the deformation patterns at the point of material separation. Electron backscatter diffraction (EBSD) was used to characterize grain texturing and grain boundaries, while limited transmission electron microscopy (TEM) was used to identify the micromechanisms of microcrack formation.

2. Materials and methods

2.1. Processing NFA-1

NFAs are typically processed by ball milling Fe–Cr–Ti–W and Y_2O_3 powders to mechanically alloy the Y and O into solid solution. The powders are then consolidated by high temperature hot isostatic pressing or extrusion [1,5]. The NOs precipitate during hot consolidation, at sizes (d) and number densities (N) that depend on alloy composition and temperature [14]. The consolidated NFA is then typically deformation processed, both to achieve better properties and a final near net shape. In the case of NFA-1, Y was included in the melt prior to gas atomization and rapid solidification. This was intended to explore the possibility of minimizing the ball-milling step and to produce more uniform distributions of NOs. ATI Powder Metals (Pittsburgh, PA) provided the atomized Fe-14Cr-3W-0.4Ti-0.2Y powders with a controlled range of O contents. However, the Y was found to be phase-separated after atomization, hence, the powders required extensive ball milling for 40 h that was carried out by Zoz GmbH (Wenden, Germany) in a CM100b attritor mill, with a ball mass-to-charge ratio of 10:1 and ball size of 5 mm. After ball milling the Y was uniformly distributed. The final Zoz milling was carried out on a low oxygen powder. In order to optimize the composition, the atomized powders were milled with 10 mesh FeO powders to yield ≈0.125 wt% O. The powders were then sealed in a 100 mm diameter mild steel can, degassed at 400 °C, and hot extruded at 850 °C through a 64x30 mm^2 rectangular die. The extruded bar was annealed for 1 h and then hot cross-rolled to an ≈50% thickness reduction, both at 1000 °C, to form an ≈15 mm thick section including the can, containing an ≈10 mm NFA-1 plate.

2.2. Characterization of the grain structure and coarse scale microstructures in NFA-1

The grain structure of the NFA-1 was evaluated in the three plate sections, designated as LT (face), LS (side, parallel to the rolling direction) and TS (front, perpendicular to the rolling direction), as illustrated in Fig. 1. The characterization toolkit primarily included: a) SEM on an FEIx30, equipped with energy dispersive spectroscopy (EDS); b) SEM on a dual beam Scanning Electron Microscope/Focused Ion Beam (SEM/FIB) FEI Helios 600; and, c) electron backscatter diffraction (EBSD) on an FEI Quanta 400F SEM. Typical sample preparation steps included 1500 grit grinding and polishing with 20 nm colloidal silica. Some of the polished samples were etched with Kroll's reagent (92% distilled water, 6% nitric acid, and 2% hydrofluoric acid). The longest (l) and shortest (s) dimensions of minimum 500 individual grains were tabulated from the SEM and SEM/FIB micrographs using 'ImageJ64' software. The nominal grain size was taken as d=(l+s)/2 and the

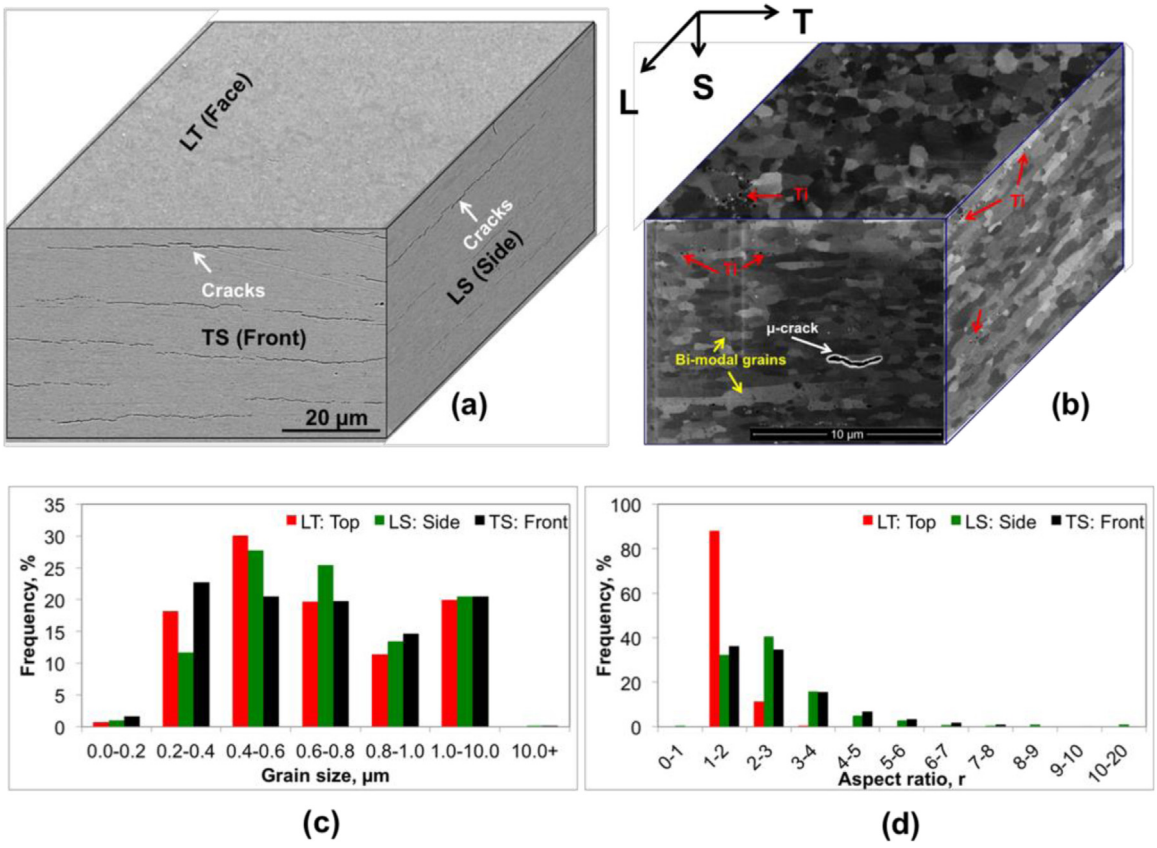

Fig. 2. NFA-1 microstructures for various plate sections: (a) SEM at lower magnification; (b) SEM/FIB at higher magnification. Fig. 2c and d show the corresponding distribution of grain size, and aspect ratio, respectively.

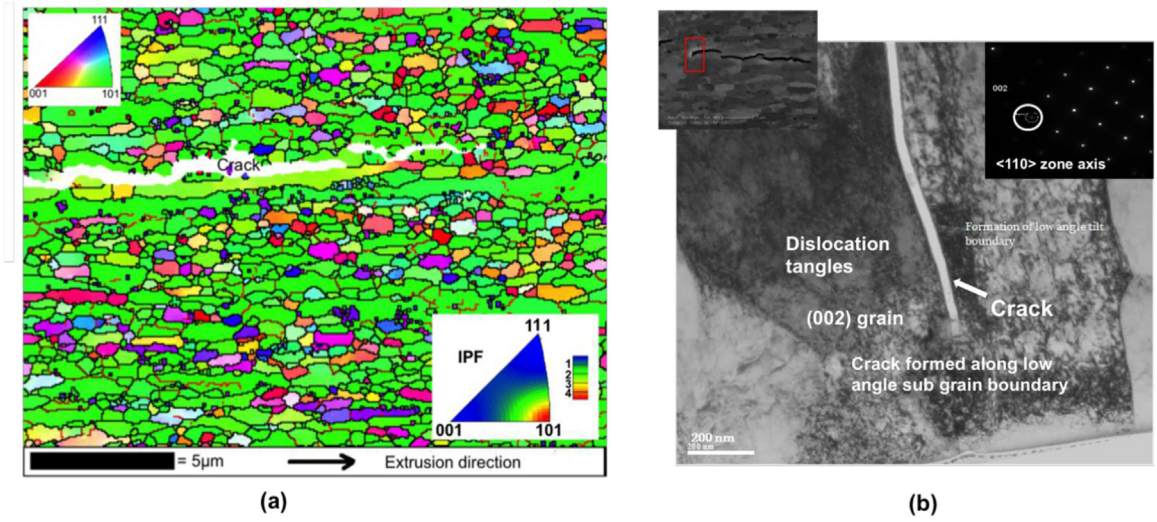

Fig. 3. (a) EBSD IPF map and intensity projection (bottom right insert) for the plate side section (LS) show a strong $<110>$ fiber texture in the extrusion direction; and, (b) FIB lift-out bright field TEM image of a crack initiation region (top-left insert) shows a microcrack running along a subgrain boundary on a {001} plane and in a $<110>$ direction. Top-right insert is the selected area diffraction (SAD) pattern using the (002) reflection.

aspect ratio as r=l/s. EBSD (parameters: voltage: 20 KeV, spot size: 4, step size: 0.05 μm and working distance: 10 mm) was used to characterize the textures induced by hot extrusion and cross-rolling. SEM and TEM, both equipped with EDS, were used to characterize the coarser-scale precipitates and microcracks [20,21]. SEM was also used extensively to characterize the fracture surfaces, tensile deformation, cracking patterns, and delamination.

2.3. Mechanical testing

Vickers microhardness measurements (H_v) were performed on polished surfaces of the various plate sections at a 500 g load using a LECO M-400A semi-automated testing instrument. A total of 10–15 indents were made in all cases in accordance with ASTM test standard E384-11e1 [22].

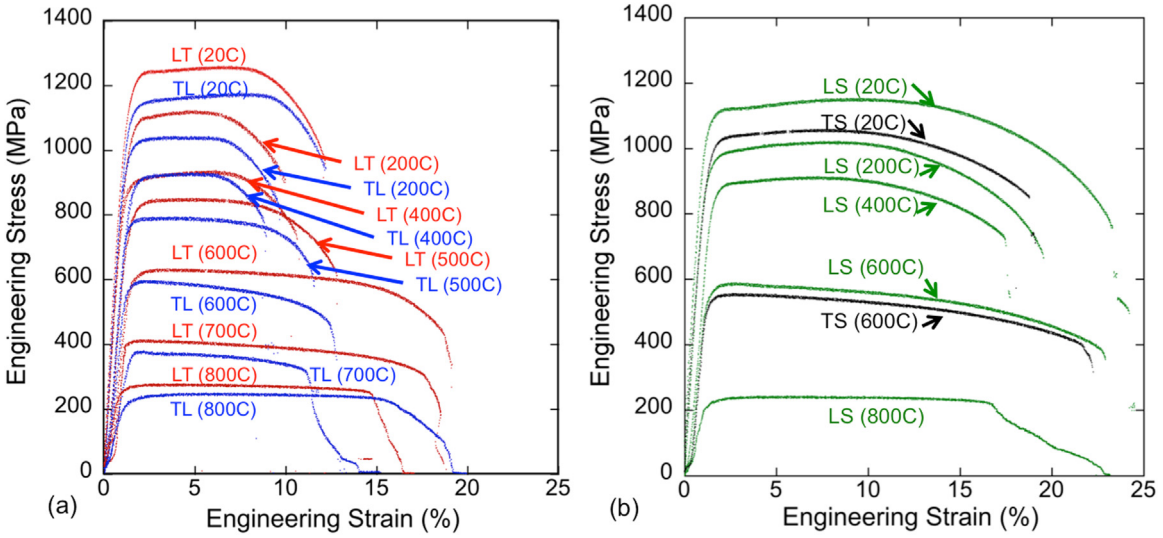

Fig. 4. Engineering stress-strain curves as a function of temperature and orientation for: (a) LT and TL; and, (b) LS and TS.

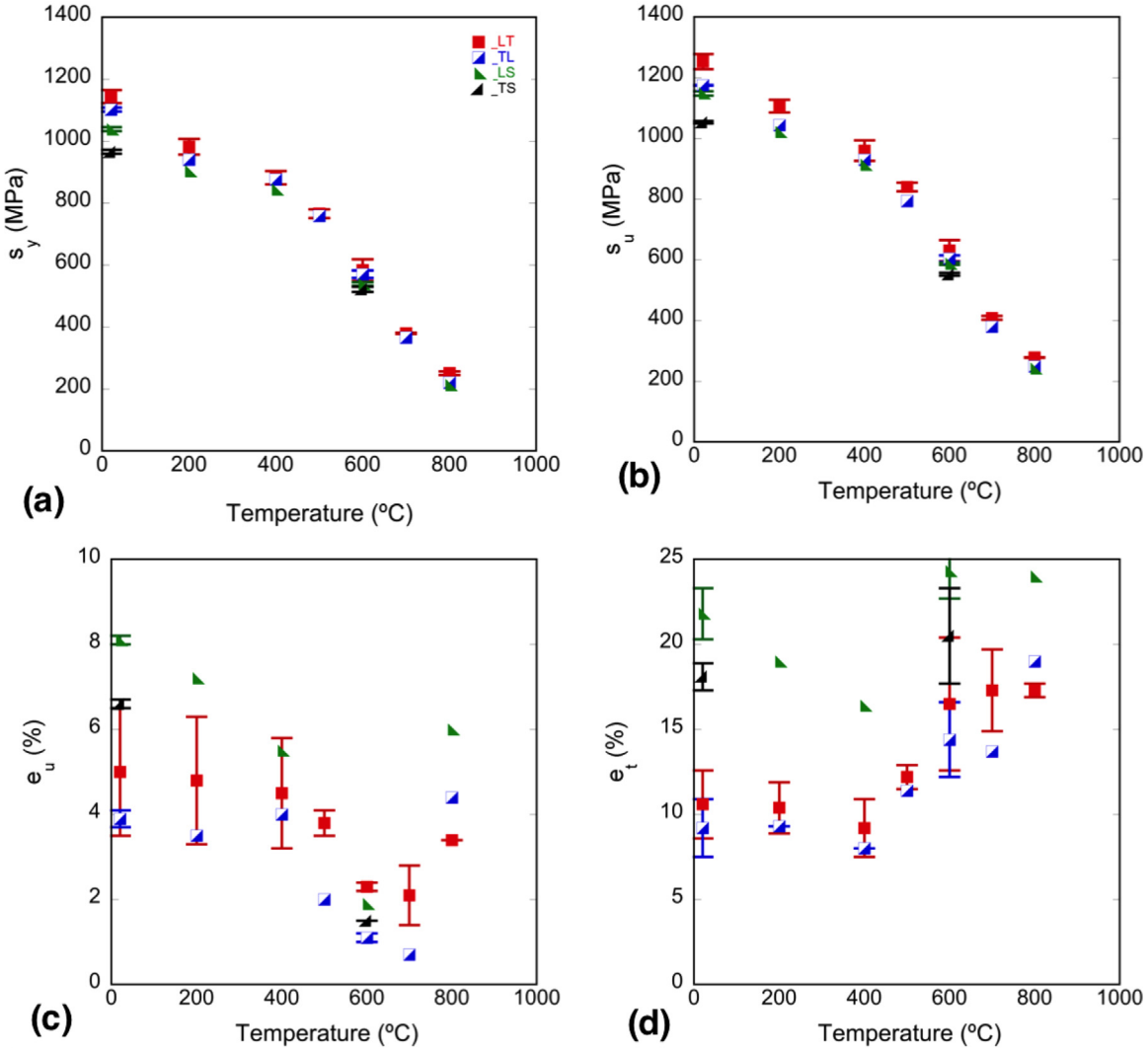

Fig. 5. NFA-1 strength and ductility as a function of temperature for: (a) the 0.2% yield stress, s_y; (b) the ultimate tensile stress, s_u; (c) uniform elongation, e_u; and, (d) total elongation, e_t. Red square: LT, blue square: TL, green triangle: LS, and black triangle: TS orientations, respectively.

Table 3
A tabulation of the tensile properties of NFA-1 as a function of temperatures and orientation.

Temp. (°C)	Orientations	s_y (MPa)	s_u (MPa)	e_u (%)	e_t (%)	RA (%)
20	LT	1144 ± 21	1253 ± 25	5.0 ± 1.5	10.6 ± 2.0	52 ± 2
	TL	1102 ± 6	1175 ± 1	3.9 ± 0.2	8.4 ± 1.4	51 ± 3
	LS	1039 ± 6	1148 ± 7	8.1 ± 0.1	21.8 ± 1.5	74 ± 13
	TS	966 ± 6	1053 ± 4	6.6 ± 0.1	18.1 ± 0.8	71 ± 6
200	LT	982 ± 25	1106 ± 21	4.8 ± 1.5	10.4 ± 1.5	56 ± 2
	TL	940	1043	3.5	9.3	54
	LS	903	1021	7.2	19	57
400	LT	882 ± 21	960 ± 34	4.5 ± 1.3	9.2 ± 1.7	49
	TL	876	930	4.0	8.0	50
	LS	844	913	5.5	16.4	47
500	LT	766 ± 14	840 ± 14	3.8 ± 0.3	12.2 ± 0.7	51
	TL	758	793	2.0	11.4	42
600	LT	584 ± 35	630 ± 35	2.3 ± 0.1	16.5 ± 3.9	62
	TL	570 ± 12	604 ± 11	1.1 ± 0.1	14.4 ± 2.2	47 ± 3
	LS	539 ± 6	587 ± 3	1.9 ± 0.2	24.3 ± 1.6	52 ± 2
	TS	522 ± 8	552 ± 5	1.5 ± 0	20.5 ± 2.8	46 ± 0
700	LT	379 ± 2	409 ± 6	2.1 ± 0.7	17.3 ± 2.4	31
	TL	366	379	0.7	13.7	35
800	LT	251 ± 6	278 ± 1	3.4 ± 0.0	17.3 ± 0.4	30
	TL	221	249	4.4	19.0	31
	LS	213	242	6	24	42

s_y=yield stress, s_u=ultimate tensile stress, e_u=uniform elongation, e_t=total elongation, and RA=reduction of area.

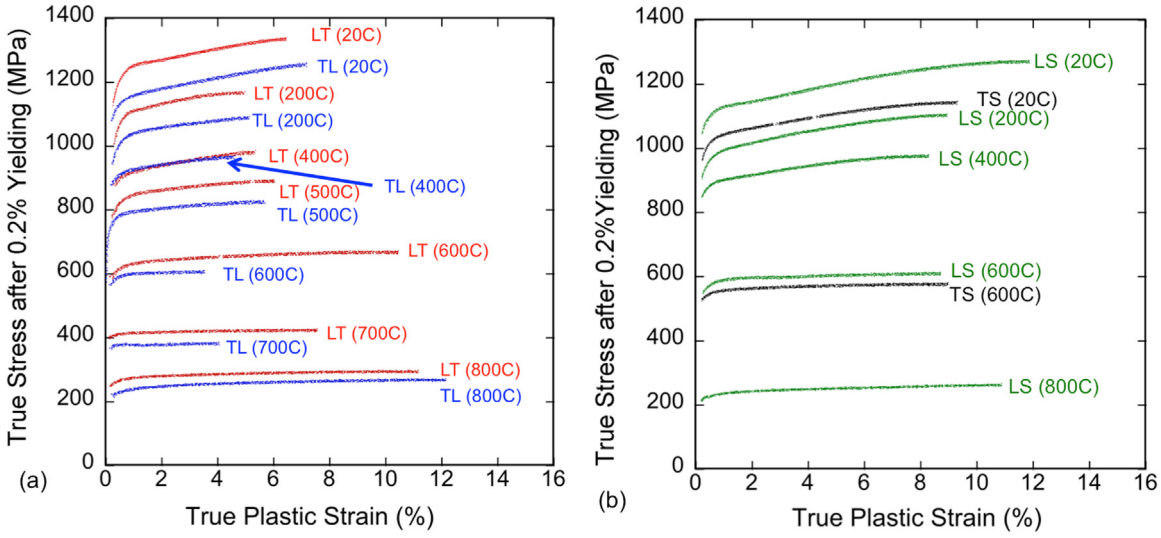

Fig. 6. True stress-true plastic strain curves as a function of temperature and orientation for: (a) LT and TL; and, (b) LS and TS.

Tensile tests were performed on dog bone shaped and sub-sized flat specimens with a nominal gauge section of $5.0 \times 1.2 \times 0.5$ mm^3 [23] in four different orientations designated as LT, TL, LS and TS, as illustrated in Fig. 1. Here the first letter designates the tensile axis orientation parallel (L) or transverse (T) with respect to the extrusion direction; while the second letter designates the plane of the plate that the specimen was extracted from – either the broad face (L or T) or short plate thickness S front or side. Thus there are 4 specimen orientations designated as LT and TL (for the face), and LS and TS (for the side). The tensile specimens were cleaned with 1500 grit paper to remove surface oxidation and damage caused by the electrical discharge machining (EDM). A MTS 810 servo-hydraulic universal testing machine equipped with a clam shell furnace was used to conduct the tests in air at temperatures ranging from ambient (≈ 22 °C) to 800 °C. Note, the TS orientation was tested only at ambient temperature and 600 °C. The specimens were heated to the target temperature and held for 10 min before loading at a displacement rate of 0.30 mm/min, or a strain rate $\approx 10^{-3}$/s. A high temperature extensometer, with ceramic arms extending into the furnace, was used to measure grip-to-grip displacement. Tensile properties were generally determined in accordance with ASTM test standard E8M-13 [24].

3. Results and discussion

3.1. Microstructural characterization

The dimensions of the grains and their distribution from different sections (i.e. LT - face, LS - side and TS - front) of the extruded and cross-rolled NFA-1 plate are shown in Tables 1 and 2 and Fig. 2. Figs. 2a and b show the low magnification SEM, and high magnification SEM/FIB images, respectively, of the as-

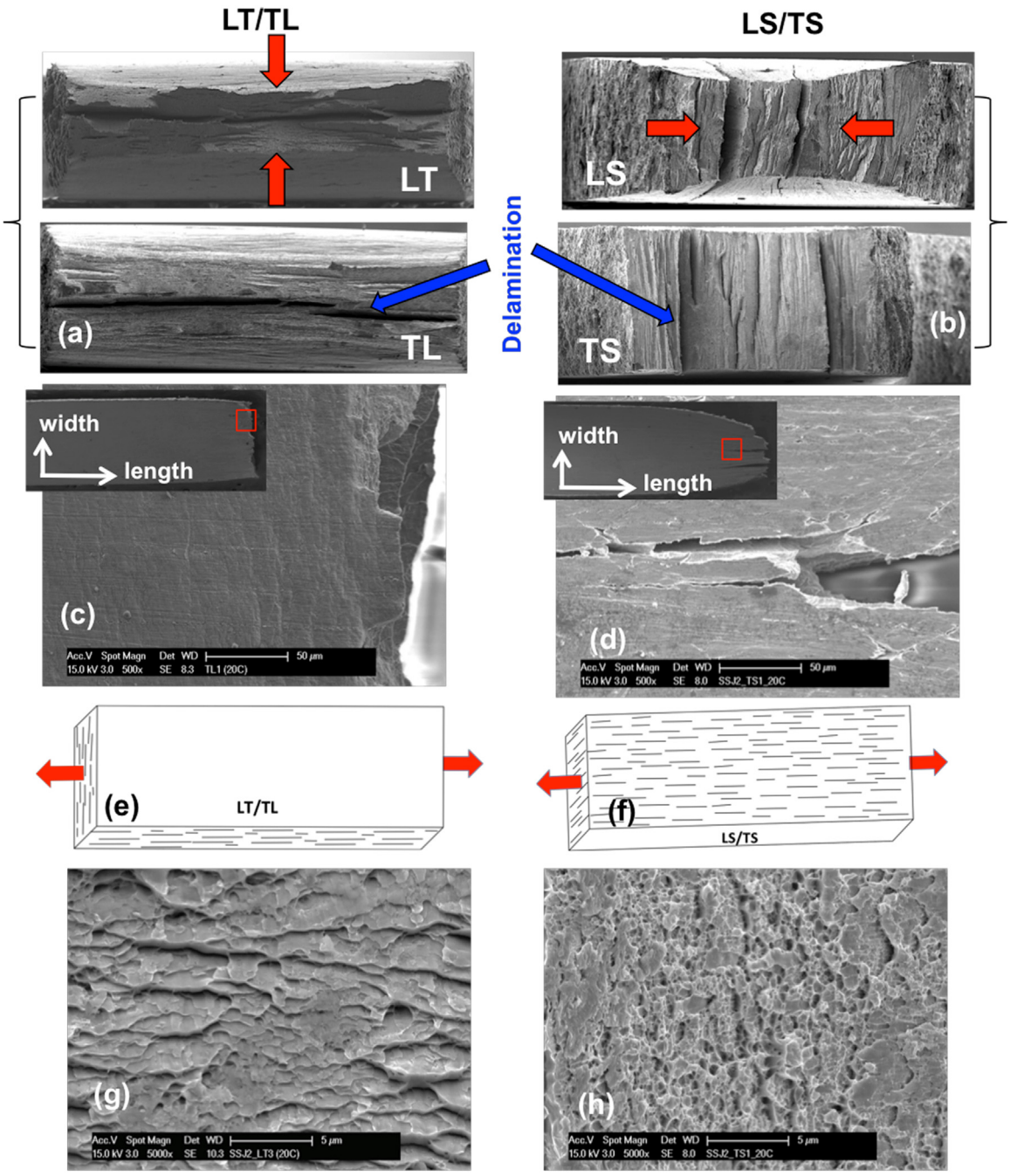

Fig. 7. Images of NFA-1 tensile specimens tested at ambient temperature: (a–b) low magnification macro views of a fracture surface; (c–d) macro (insert) and higher magnification views of a tensile specimen side surface, marked by the boxed; (e–f) schematic of the microcracks in the two orientations; and, (g–h) high magnification images of ductile fracture surfaces for LT and TL, as well as LS and TS, orientations. Note that all the inserted macro-views show the length (horizontal direction), and width (vertical direction), as well as the fractured edge, of the tensile specimen.

fabricated and pre-test NFA-1 for different planes. The plate faces (LT) are crack-free, with nearly uniform, equiaxed, ultrafine grains (see Table 1). In contrast, the side (LS), and front (TS) sections reveal a large number of microcracks on planes parallel to the plate faces and normal to the short thickness direction. The corresponding grains are pancake-shaped and elongated in the extrusion (LS) and cross-rolling (TS) directions. A bimodal grain size distribution (most are in sub-micron range, others are in micron size range with a small number of grains larger than 10 μm) is also observed (see Table 2 and Fig. 2c). The pancake-shaped grain aspect ratio (GAR) varies from ≈ 2-16; the GAR distribution is shown in Fig. 2d. The fraction of submicron grains is ≈ 80%, representing ≈ 60% area fraction (see Table 2). A through-thickness grain size variation is also observed, with thinner grains found near plate faces and relatively thicker grains in the middle. Most as-fabricated NFAs exhibit bimodal grain size distributions, especially at higher processing temperatures. In some cases large grains can indicate a low number density of NOs. In this alloy, however, the Y is uniformly distributed, likely due to inclusion during the atomization step, and high number densities of NOs are observed in both the nano- and micron-sized grains. The precursor alloys to NFA-1 have also shown this behavior and large grains with NOs have also been observed by other research groups [25].

Coarse Ti- and Y-rich oxides stringers are also observed (Fig. 2b). Examination of 150-270 oxide particles showed that they ranged in size from ≈ 10 nm to 260 nm, averaging ≈ 60 nm. These

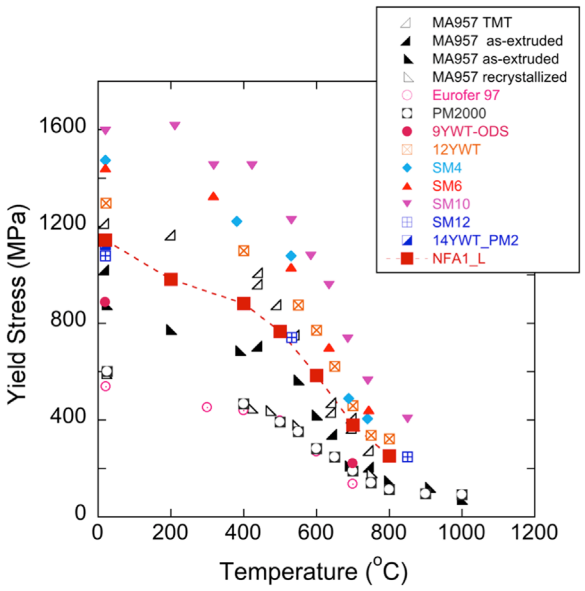

Fig. 8. The 0.2% yield strength of various NFA steels as a function of temperature compared to NFA-1 [1,4,5,10,11,13,17,28,29,34,35].

coarser oxides are predominantly located at or near prior particle grain boundaries (Fig. 2b). Such features are common in NFA/ODS alloys [26]. Fig. 2 also shows the presence of microcracks running normal to the plate thickness direction in both the side (LS) and front (TS) plate views. The average opening, at the presumed initiation point roughly at the crack center, is ≈ 250 nm. The crack separation distance in the short thickness direction is ≈ 16 μm. The crack lengths range from 2 to 105 μm averaging ≈ 10 μm (side section) to 15 μm (front section). Detailed descriptions of the statistics of the coarser precipitates and cracks are reported elsewhere [21].

Fig. 3a shows an EBSD inverse pole figure (IPF) map for a section of the LS (side) surface. The map is color-coded to show the grain orientation texturing in the extrusion direction. As expected, most of the grains have a near $<110>$-fiber texture in the extrusion direction. This texturing is also shown in the IPF intensity projection in the bottom right insert of Fig. 3a. The EBSD map also shows one large and one small crack parallel to the extrusion direction, although they may be linked below the surface.

The texturing is accompanied by the development of {001} planes normal to the thickness direction. Notably the resulting $\{100\}<011>$ texture represents the most brittle cleavage system in BCC Fe. The $\{001\}<001>$ sessile dislocations are formed by the reaction of $<111>$ type dislocations and produce sessile low-angle subgrain boundaries on {100} planes. Further deformation results in dislocation pile-ups at the subgrain boundaries, creating local stress concentrations and opening displacements that form microcracks for the brittle $\{100\}<110>$ cleavage system (Fig. 3b). The bright field (BF) TEM image of a FIB lift-out lamella (Fig. 3b), prepared perpendicular to the crack initiation front (top-left insert of Fig. 3b), shows dislocation tangles around the crack and a microcrack running along a subgrain boundary on a {001} plane in a $<110>$ direction. Microcrack propagation is also partly driven by residual stresses that develop during deformation. The detailed mechanisms of texturing and microcrack formation in the NFA-1 plate are discussed elsewhere [20].

3.2. 14YWT strength

Vickers microhardness (H_v) data for NFA-1 is summarized in Table 1. The H_v averages 376 ± 18, 368 ± 25 and 352 ± 39 (kg/mm^2) on the plate face, side and front, respectively. The differences, of up to ~6%, are probably not statistically significant. However, the higher standard deviation and lower value of H_v for the plate front and side is likely due to delamination, which is discussed below.

Engineering stress-strain or s(e) curves for the various orientations over a wide range of temperatures are shown in Fig. 4. The average values of the engineering yield (s_y) and ultimate (s_u) stresses are plotted in Fig. 5a and b, respectively, while the corresponding uniform (e_u) and total (e_t) elongations are shown in Fig. 5c and d, respectively. Table 3 summarizes the average and standard deviations of the tensile properties as a function of temperature and orientation. Note s_y was determined at the standard nominal 0.2% offset. Note the differences in s(e) in the elastic regime are due to temperature-dependent compliance of the specimen and fixture coupling and the initial low load displacements. Fig. 6 plots the true stress (σ) versus true plastic strain (ε) curves starting at the nominal 0.2% offset.

The LT orientation at ambient temperature (AT) exhibits the highest $s_y \approx 1144 \pm 21$ MPa and $s_u \approx 1253 \pm 25$ MPa, accompanied by $e_u \approx 5.0 \pm 1.5\%$ and $e_t \approx 10.6 \pm 2.0\%$, respectively. The TL orientation generally showed similar strength and ductility. However, the s_y and s_u in the LS and TS orientations are slightly lower ($\approx 10\%$), while their corresponding e_t values are much larger. These differences arise from a combination of texturing, varying grain dimensions and the presence of microcracks and delamination.

As illustrated in Fig. 7a, the LT and TL orientations delaminate, forming splits in the dog bone coupon specimen thickness dimension, propagating parallel to the gauge section width. In the case of the LS and TS orientations multiple delaminations split the width of the gauge section, propagating parallel to the thickness dimension as seen in Fig. 7b and d. One effect of the 90° delamination LT/TL and LS/TS rotation is to lower the lateral stresses, perhaps reducing slightly any triaxial constraint effects. Indeed the s(e) curves in Fig. 4b show possible reductions in the necking constraint in the width direction. Fig. 7e and f show a schematic of the microcracks in the two cases. The higher magnification SEM images of fracture surface in the plate face orientation (LT or TL) show large flat-bottomed features, separated by shear lips (Fig. 7g). In contrast, Fig. 7h shows more classical, fine scale ductile-dimple fracture surfaces. The scale of the damage is related to the geometry of the microcracks and specimen width versus thickness. When the microcrack planes are parallel to the gauge section width (LT – broad faces) the scale of damage appears coarser, while the corresponding scale appears finer when the microcracks are parallel to the gauge section thickness (LS or TS - thin faces).

Thus, while the s(e) curves are primarily controlled by the actual intrinsic material properties of NFA-1, pre-existing microcrack damage and extrinsic factors, like the dog bone coupon tensile specimen geometry, also play a role. Better understanding of how the mix of texturing, damage and extrinsic factors govern tensile deformation of NFA-1 will be investigated in future studies. These studies will be based on finite element simulations, which we routinely use to extract post-necking true $\sigma(\varepsilon)$ constitutive laws [9,27] from tensile test s(e) data. The future simulations will treat all of the extrinsic factors noted above. However, further discussion of this complex topic is beyond the scope of this paper.

As is common with NFAs and other steels, the s_y and s_u decrease relatively slowly between ambient temperature and ≈ 400 °C. This is primarily due to the corresponding decrease in the shear modulus [1,28,29]. The strength of NFA-1 is controlled by contributions from: (a) Hall-Petch grain boundary strengthening; (b) dislocation pinning by NOs; (c) network dislocation and subgrain structures; and, (d) solid solution matrix hardening

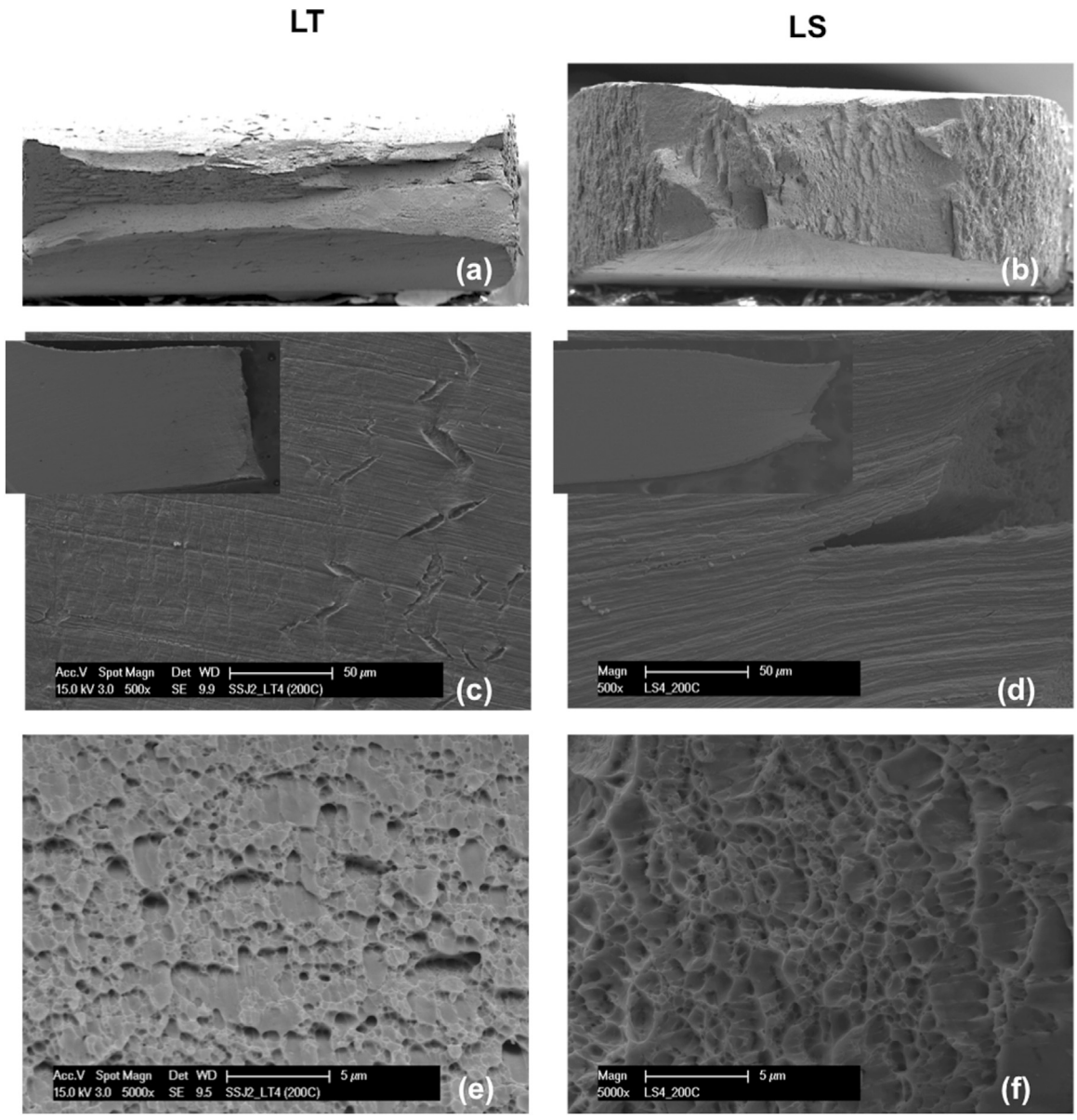

Fig. 9. Images of NFA-1 LT (left) and LS (right) tensile specimens tested at 200 °C showing: (a–b) macro views of a fracture surface; (c–d) macro (insert) and higher magnification views of a tensile specimen side surface; and, (e–f) high magnification images of ductile fracture surfaces. See text for a discussion.

[1,5,26,30]. The s_y and s_u decrease more rapidly above 500 °C due to a variety of thermally activated processes, including dislocation bypass mechanisms associated with de-pinning from the NOs. Above 600 °C deformation is dominated by viscoplastic creep, even at relatively high strain rates [1,29–31]. Creep is indicated by the almost constant true σ seen in the post-transient $\sigma(\varepsilon)$ curves in Fig. 6. In the creep regime, the stress at an imposed strain rate (ε') and given temperature is governed by a threshold stress (σ_t) power law dislocation mechanisms as [5,32]

$$\varepsilon' = C\exp(-Q_c/RT)(\sigma - \sigma_t)^n.$$

Here Q_c is the creep activation energy. The σ_t is a significant fraction of the dislocation obstacle-strengthening component of the static σ_y. A more detailed discussions of NFA creep properties and processes can be found elsewhere [1,5,33] and will be described for NFA-1 in future publications. Again this paper focuses on nominal strain rate ($\approx 10^{-3}$) quasi-static tensile properties.

In spite of the strength decrease above 400 °C, NFA-1 remains strong at higher temperatures, with s_y and s_u of 584 ± 35 MPa and 630 ± 35 MPa at 600 °C and 251 ± 6 and 278 ± 1 MPa at 800 °C, respectively (Table 3 and Fig. 5). Notably, NFA-1 retains ≈22% of its ambient temperature strength up to ~2/3 T_m, hence qualifies as a ferritic superalloy [1].

Fig. 8 compares the s_y of NFA, ODS and RAFM steels at different temperatures for the LT orientation [1,4,5,10,11,13,17,28,29,34,35]. The s_y for NFA-1 falls roughly in the middle of the strength band for the broad class of NFA representing a wide range of deformation-heat treatment conditions. It is noted that a series of earlier SM plates produced at ORNL range from slightly stronger to much stronger than NFA-1. A Japanese 12WYT also shows higher strength than NFA-1.

Along with high s_y and s_u, NFA-1 maintains good tensile ductility over a wide range of temperature, as summarized in Table 3 and Fig. 5. The e_u is highly anisotropic, generally being highest in the LS orientation, where it ranges from ≈1.9-8.1 ± 0.1% with a minimum at 600 °C. The e_u is lowest in the TL orientation, with a minimum at 700 °C of 0.7% and a maximum of 4.4% at 800 °C. A

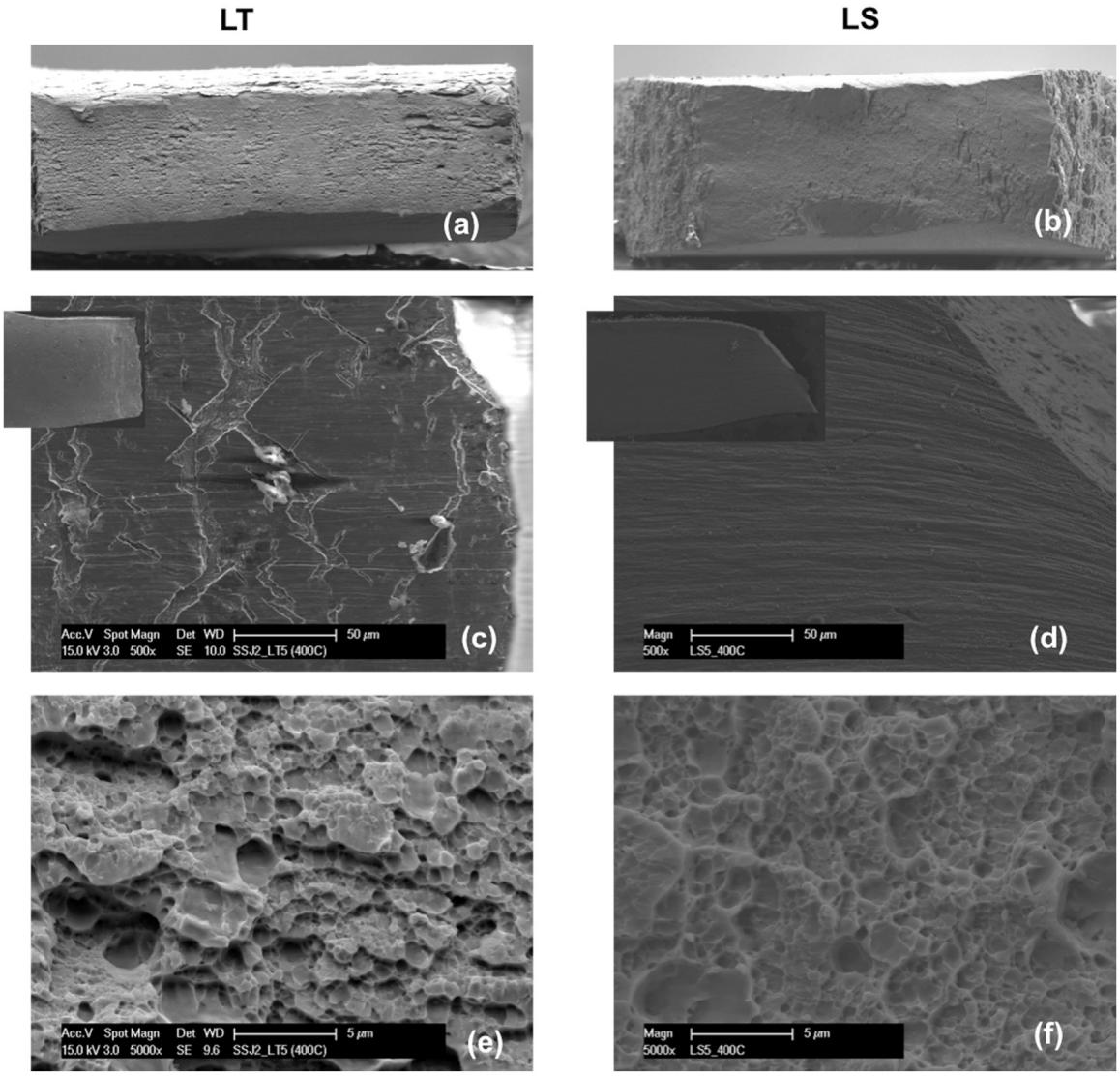

Fig. 10. Images of NFA-1 LT (left) and LS (right) tensile specimens tested at 400 °C showing: (a–b) macro views of a fracture surface; (c–d) macro (insert) and higher magnification views of a tensile specimen side surface; and (e–f) high magnification images of ductile fracture surfaces. See text for a discussion.

generally similar pattern is observed in the e_t, although the minimum occurs at 400 °C in this case, and the total strain varies less with temperature, ranging from a minimum of 8.0% (TL at 400 °C) to the maximum of 24.3% (LS at 600 °C).

3.3. *Tensile fracture deformation, cracking and fracture surface observations*

The room temperature tensile fracture surfaces shown in Fig. 7 reveal different morphologies for LT and TL versus LS and TS orientations. In all cases, the fracture surfaces are dominated by the delamination. As seen in Fig. 7a, one deep delamination crack forms in the middle of the gauge section thickness in the LT and TL orientations, along with some smaller cracks that are observed on the TL fracture surface. A profile gauge section view in Fig. 7c shows that the fracture surface is flat and is associated with only a modest reduction in width. However, both the LT and TL orientations thin extensively in the thickness direction forming two approximately knife-edge-type features surrounding the mid-section out-of-plane delamination. Together these deformation patterns yield a significant reduction in area (RA) of $\approx 52 \pm 2\%$. In contrast, as seen in Fig. 7b and d, multiple delamination cracks are observed that split the width of the LS and TS specimens. In this case, necking occurs in both the thickness and width directions, leading to a larger RA of $74 \pm 13\%$. Qualitatively, the reduction in strength and increase in ductility correlates with the number and orientation of the delaminations. This correlation could be due to relaxation of a multi-axial stress state, although it is difficult to understand in the context of a uniaxial loading prior to necking. Thus, as noted previously, more detailed finite element simulations of the tensile test are needed.

Further discussion of deformation and fracture mechanisms will focus on LT and LS since they show similar behavior to their respective TL and TS counterparts. Fig. 9 shows the fracture surfaces and profiles for tests at 200 °C. The results are generally very similar to those at ambient temperature, except for the notable absence of major delamination. The absence of delamination is due to a brittle-to-ductile transition (BDT) for microcrack cleavage fracture toughness that occurs in the 23 to 200ºC temperature interval. The DBT will be addressed in future publications, including one on tensile tests in the short plate thickness orientation where loading is normal to the microcrack planes [36]. Both e_u and e_t decrease when increasing from ambient temperature to 200 °C, with a RA of $\approx 56 \pm 2\%$ for LT and 57% for LS. Note, the RA at 200 °C in all the orientations are quite similar in the absence of delamination.

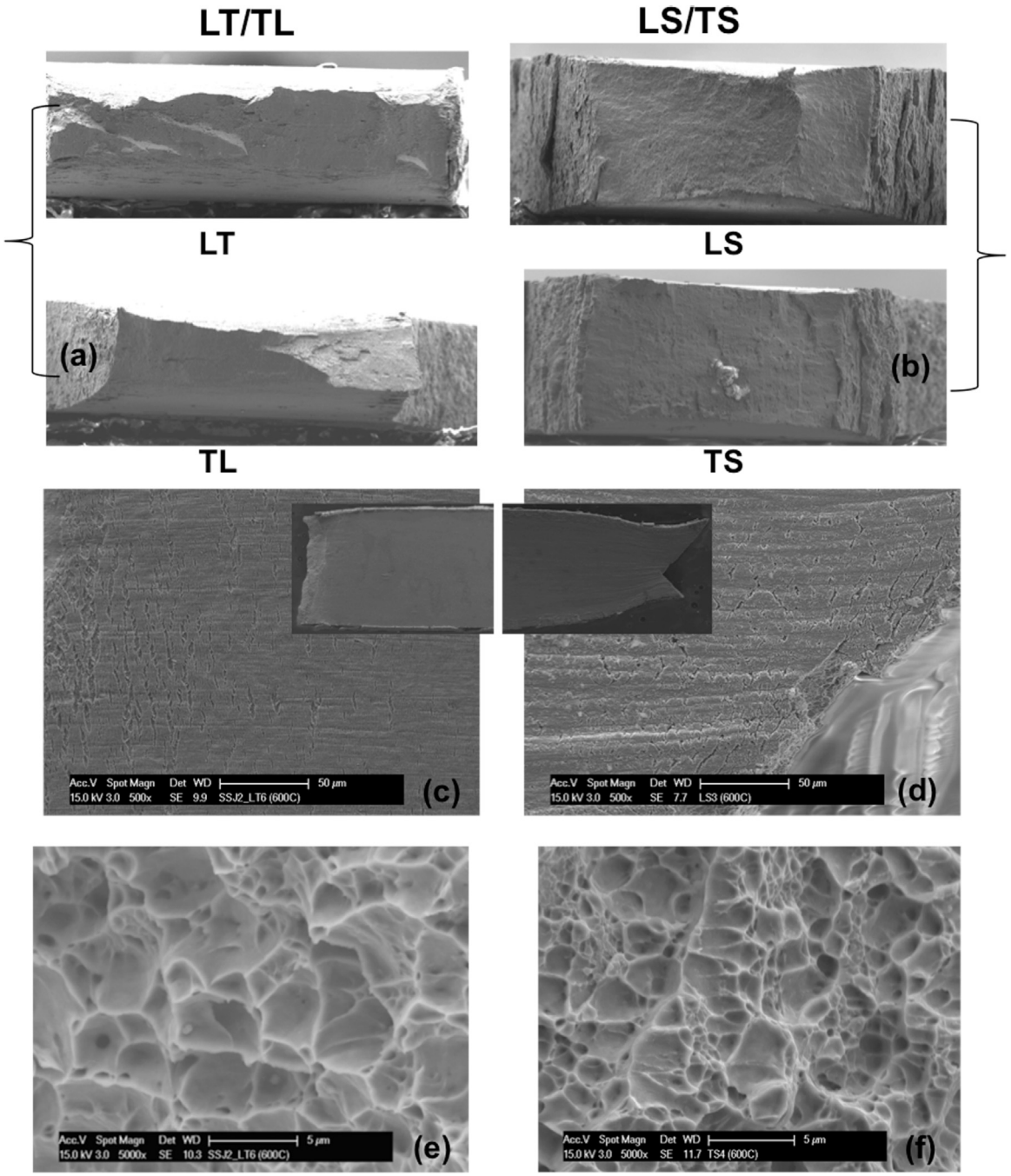

Fig. 11. Images of NFA-1 LT and TL (left), and LS and TS (right) tensile specimens tested at 600 °C showing: (a–b) macro views of a fracture surface; (c–d) macro (insert) and higher magnification views of a tensile specimen side surface; and (e–f) high magnification images of ductile fracture surfaces. See text for a discussion.

Fig. 10 shows the fracture characteristics of LT and LS at 400 °C. The LT orientation again behaves in a very similar manner to that at lower temperatures, and again with no sign of any delamination. Fracture in the LS orientation occurs by double shear, as shown in the profile view, along with a single shallow out-of-plane arrested crack. Necking occurs in both the thickness and width directions, resulting in ≈47% RA. The fracture surfaces are similar to those at lower temperature in both cases. The e_t is minimum at 400 °C, and again higher in the LS orientation. In contrast e_u is minimum at ≈700 °C. The observed temperature trend marks the transition to viscoplastic creep, starting above 400 °C. There is a generally similar e_u and e_t in both orientations, and the differences are smaller for e_u.

Fig. 11 shows the fractography results for tests at 600 °C. No delamination is observed and necking occurs in both directions, with up to ≈62% RA. The fracture surfaces again appear to be similar to those at lower temperatures. Side surface cracking normal to the loading direction near the fracture surface is still observed especially in the LS orientation. Note the side surface cracking evolves from being parallel to the loading direction at RT, a mix of 45° and normal cracks at 200–400 °C, and normal at or above 600 °C. The e_u is near minimum at 600 °C.

The specimens are too oxidized to clearly observe the fracture surfaces in detail at 800 °C. However, overall observations show that there is little necking in the tertiary creep regime, but the substantial e_u and e_t ductility is due to the extensive plastic strain in the minimum creep regime. The oxidized fracture surface appears to show a mix of smaller and larger dimple features. The

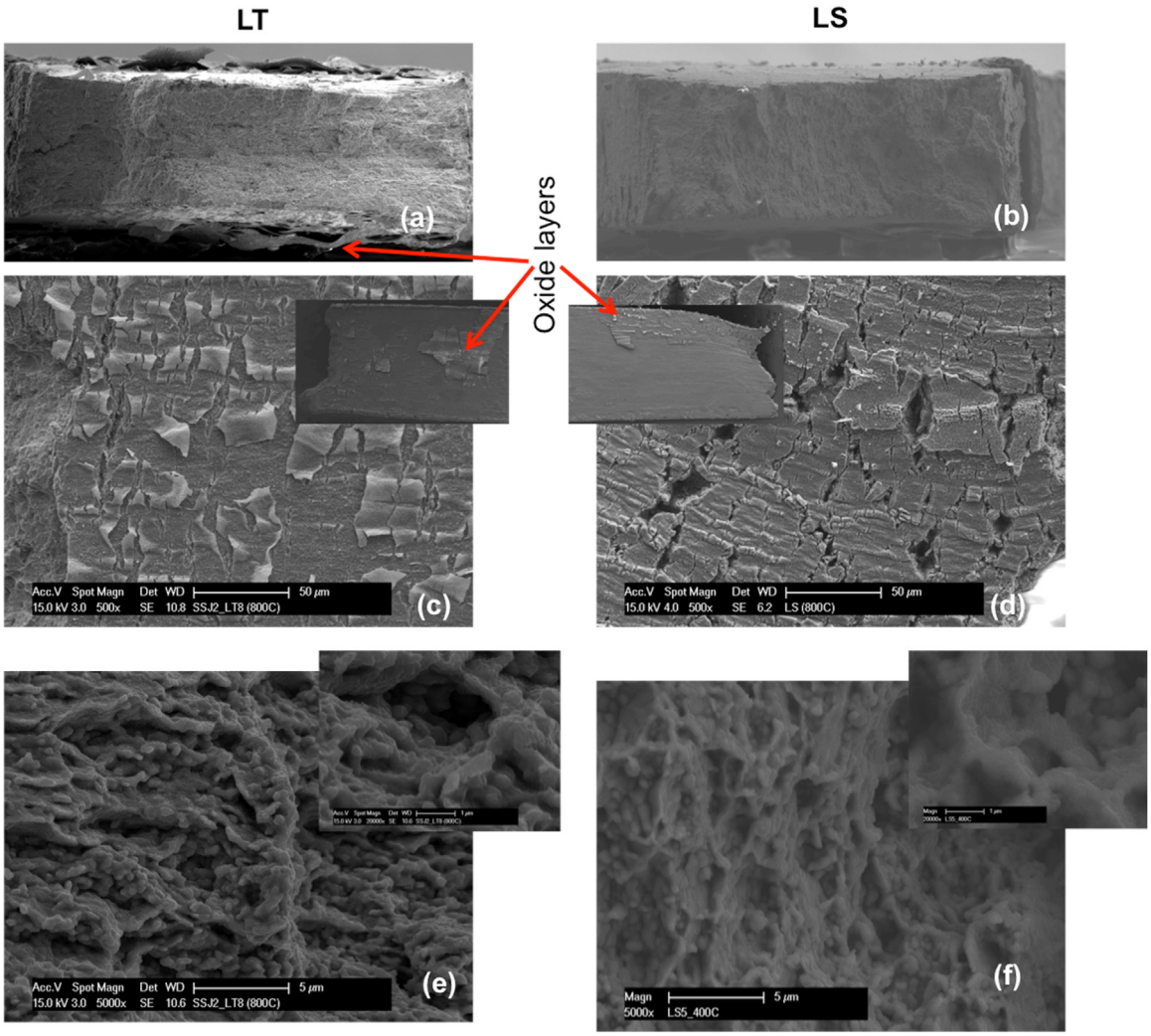

Fig. 12. Images of NFA-1 LT (left) and LS (right) tensile specimens tested at 800 °C showing: (a–b) macro views of a fracture surface; (c–d) macro (insert) and higher magnification views of a tensile specimen side surface; and (e–f) high magnification images of ductile fracture surfaces. See text for a discussion.

sidewalls of the larger features are filled with smaller dimples (Fig. 12e and f inserts).

4. Summary and conclusions

A summary of the conclusions that can be drawn from our tensile test deformation and fracture study of 14YWT NFA-1 is the following:

1. Deformation processing produces a bimodal distribution of pancake-shaped grains that are nearly equiaxed when observed on the plate surface and flattened and elongated as seen in the side sections. Small sub-μm grains are dominant, but represent only ≈60% of the grain area fraction.
2. A large population of microcracks form on planes parallel to the broad plate surfaces during extrusion and cross rolling. A more detailed description of the micro cracks and their formation mechanisms are reported elsewhere [20].
3. The microcracks lead to extensive, geometrically mediated delamination during tensile testing at lower temperatures.
4. The absence of delamination at 200ºC and above is due to a brittle-to-ductile transition for microcrack cleavage fracture toughness.
5. NFA-1 is a very strong alloy. The average ambient temperature NFA-1 microhardness ranges from 352 to 376 kg/mm^2 on the various plate faces. The ambient temperature s_y and s_u range from 966 to 1144 MPa and 1053–1253 MPa, respectfully. The absolute strength difference decreases with increasing temperature.
6. The tensile ductility parameters (e_u, e_t and RA) are much more anisotropic and temperature dependent with a minimum in e_u at ≈700 °C and in e_t at ≈400 °C. However, there is substantial RA in all cases except at 800 °C.
7. Delamination, and some extrinsic factors, play a moderate role in NFA-1 strength, and a somewhat stronger role in tensile ductility. The ductile fracture patterns are strongly affected by delamination cracking , but this decreases with increasing temperature.

Acknowledgement

The authors gratefully acknowledge the support received for this research work by the U.S. Department of Energy Office of Fusion Energy Sciences (DE-FG03-94ER54275) and the Office of Nuclear Energy university programs administered by INL (IDNL Award #00119430 8-442520-59048).

References

[1] G.R. Odette, Recent progress in developing and qualifying nanostructured ferritic alloys for advanced fission and fusion applications, JOM 66 (2014) 2427–2441.

[2] Ch.Ch Eiselt, M. Klimenkov, R. Lindau, A. Moslang, G.R. Odette, T. Yamamoto, D. Gragg, Tensile and fracture toughness properties of the nanostructured oxide dispersion strengthened ferritic alloy 13Cr-1W-0.3Ti-0.3Y_2O_3, J. Nucl. Mater. 417 (2011) 193–196.

[3] N.J. Cunningham, Y. Wu, A. Etienne, E.M. Haney, G.R. Odette, E. Stergar, D. T. Hoelzer, Y.D. Kim, B.D. Worth, S.A. Maloy, Effect of bulk oxygen on 14YWT nanostructured ferritic alloys, J. Nucl. Mater. 444 (2014) 35–38.

[4] I.S. Kim, B.Y. Choi, C.Y. Kang, T. Okuda, P.J. Maziasz, K. Miyahara, Effect of Ti and W on the mechanical properties and microstructure of 12%Cr base mechanical alloyed nano-sized ODS ferritic alloys, ISIJ Int. 43 (2003) 1640–1646.

[5] G.R. Odette, M.J. Alinger, B.D. Wirth, Recent developments in irradiation-resistant steels, Annu. Rev. Mater. Res. 38 (2008) 471–503.

[6] G.R. Odette, D.T. Hoelzer, Irradiation-tolerant nanostructured ferritic alloys: transforming helium from a liability to an asset, JOM 62 (2010) 84–92.

[7] Y. Dai, G.R. Odette, T. Yamamoto, The effects of helium in irradiated structural alloys, Compr. Nucl. Mater. 1 (2012) 141–193.

[8] M.J. Alinger, G.R. Odette, G.E. Lucas, Tensile and fracture toughness properties of MA957: implications to the development of nanocomposited ferritic alloys, J. Nucl. Mater. 307–311 (2002) 484–489.

[9] S.A. Maloy, T.A. Saleh, O. Anderoglu, T.J. Romero, G.R. Odette, T. Yamamoto, J. I. Cole, R. Fielding, Characterization and comparative analysis of the tensile properties of five tempered martensitic steels and an oxide dispersion strengthened ferritic alloy irradiated at $\approx$295 °C to–6.5 dpa, J. Nucl. Mater. 468 (2016) 232–239.

[10] D.T. Hoelzer, K.A. Unocic, E.T. Manneschmidt, M.A. Sokolov, Reference characterization of the advanced ODS 14YWT-SM12 heat used in HFIR JP30/31 neutron irradiation experiment, Fusion Materials Semiannual Progress Report for Period Ending June 30, 2012, DOE/ER-0313/52, U.S. Department of Energy, 52, 2012, pp. 33–46.

[11] D.A. McClintock, D.T. Hoelzer, M.A. Sokolov, R.K. Nanstad, Mechanical properties of neutron irradiated nanostructured ferritic alloy 14WYT, J. Nucl. Mater. 386–388 (2009) 307–311.

[12] T.S. Byun, J.H. Yoon, S.H. Wee, D.T. Hoelzer, S.A. Maloy, Fracture behavior of 9Cr nanostructured ferritic alloy with improved fracture toughness, J. Nucl. Mater. 449 (2014) 39–48.

[13] D.T. Hoelzer, J. Bentley, M.A. Sokolov, M.K. Miller, G.R. Odette, M.J. Alinger, Influence of particle dispersions on the high-temperature strength of ferritic alloys, J. Nucl. Mater. 367–370 (2007) 166–172.

[14] M.J. Alinger, G.R. Odette, D.T. Hoelzer, On the role of alloy composition and processing parameters in nanocluster formation and dispersion strengthening in nanostructured ferritic alloys, Acta Mater. 57 (2009) 392–406.

[15] J.H. Kim, K.M. Kim, T.S. Byun, D.W. Lee, C.H. Park, High-temperature oxidation behavior of nanostructured ferritic oxided dispersion-strengthened alloys, Thermochim. Acta 579 (2014) 1–8.

[16] P. Miao, G.R. Odette, T. Yamamoto, M. Alinger, D. Hoelzer, D. Gragg, Effects of consolidation temperature, strength and microstructure on fracture toughness of nanostructured ferritic alloys, J. Nucl. Mater. 367–370 (2007) 208–212.

[17] N.J. Cunningham, Y. Wu, G.R. Odette, D. Gragg, K. Field, D.T. Hoelzer, S.A. Maloy, Characterization of the final precursor alloy to a larger best practice heat of 14YWT, Fusion Materials Semiannual Progress Report for Period Ending December 31, 2012, DOE/ER-0313/53, U.S. Department of Energy, 53, 2012, pp. 20–33.

[18] N.J. Cunningham, Y. Wu, G.R. Odette, D.T. Hoelzer, S.A. Maloy, Characterization of a larger best practice heat of 14YWT in annealed powder, HIP consolidated and extruded forms, Fusion Materials Semiannual Progress Report for Period Ending June 30, 2013, DOE/ER-0313/54, U.S. Department of Energy, 54, 2013, pp. 15–26.

[19] M.E. Alam, N.J. Cunningham, D. Gragg, K. Fields, G.R. Odette, D.T. Hoelzer, S.A. Maloy, Mechanical Properties Characterization of a Larger Best Practice Heat of 14YWT NFA1, Fusion Materials Semiannual Progress Report for Period Ending June 30, 2014, DOE/ER-0313/56, U.S. Department of Energy, 56, 2014, pp. 63–69.

[20] S. Pal, M.E. Alam, G.R. Odette, D. Hoelzer, S. Maloy, Microstructure, texturing, microcracking and delamination behavior of NFA-1, Fusion Materials Semiannual Progress Report for Period Ending June 30, 2015, DOE/ER-0313/58, U.S. Department of Energy, 58, 2015, pp. 66–82.

[21] M.E. Alam, S. Pal, D. Gragg, G.R. Odette, D.T. Hoelzer, S.A. Maloy, Microstructural and Mechanical Behavior of as-fabricated and Annealed 14YWT NFA-1 Alloy, Fusion Materials Semiannual Progress Report for Period Ending December 31, 2015, DOE/ER-0313/59, U.S. Department of Energy, 59, 2015, pp. 35–46.

[22] A.S.T.M. E384-11e1, Standard Test Method for Knoop and Vickers hardness of Materials, ASTM International, West Conshohocken, PA, 2011.

[23] H. Je, Stress Corrosion Cracking Behavior of Oxide Dispersion Strengthened Ferritic Steel in Supercritical Pressurized Water (Ph.D thesis), Kyoto University, Japan 2013, p. 109.

[24] ASTM E8/E8M-13, Standard test methods for tension testing of metallic materials, ASTM International, West Conshohocken, PA, 2013.

[25] Ch.Ch Eiselt, M. Klimenkov, R. Lindau, A. Moslang, Characteristics results and prospects of the 13Cr-1W-0.3Ti-0.3Y2O3 ODS steel, J. Nucl. Mater. 386–388 (2009) 525–528.

[26] N.J. Cunningham, Study of the Structure, Composition, and Stability of Y–Ti–O nm-scale Features in Nanostructured Ferritic Alloys (Ph.D thesis), UCSB, USA, 2012.

[27] T. Yamamoto, G.R. Odette, M.A. Sokolov, On the fracture toughness of irradiated F82H: effects of loss of constraint and strain hardening capacity, J. Nucl. Mater. 417 (2011) 115–119.

[28] R.L. Klueh, J.P. Shingledecker, R.W. Swindeman, D.T. Hoelzer, Oxide dispersion-strengthened steels: a comparison of some commercial and experimental alloys, J. Nucl. Mater. 341 (2005) 103–114.

[29] J.H. Kim, T.S. Byun, D.T. Hoelzer, S.W. Kim, B.H. Lee, Temperature dependence of strengthening mechanisms in the nanostructured ferritic alloy 14YWT: part I-Mechanical and microstructural observations, Mater. Sci. Eng. A 559 (2013) 101–110.

[30] J.H. Kim, T.S. Byun, D.T. Hoelzer, C.H. Park, J.T. Yeom, J.K. Hong, Temperature dependence of strengthening mechanisms in the nanostructured ferritic alloy 14YWT: Part II-Mechanistic models and predictions, Mater. Sci. Eng. A 559 (2013) 111–118.

[31] A. Steckmeyer, M. Praud, B. Fournier, J. Malaplate, J. Garnier, J.L. Béchade, I. Tournié, A. Tancray, A. Bougault, P. Bonnaillie, Tensile properties and deformation mechanisms of a 14Cr ODS ferritic steel, J. Nucl. Mater. 405 (2010) 95–100.

[32] D.J. Srolovitz, R.A. Petkovic-Luton, M.J. Luton, Diffusion relaxation of the dislocation-inclusion repulsion, Philos. Mag. A 48 (1983) 795–809.

[33] S. Ukai, T. Okuda, M. Fujwara, T. Kobayashi, S. Mizuta, H. Nakashima, Characterization of high temperature creep properties in recrystallized 12Cr-ODS ferritic steel claddings, J. Nucl. Sci. Technol. 39 (2002) 872–879.

[34] T.S. Byun, D.T. Hoelzer, G.R. Romanosky, D.A. McClintock, Thermochemical behavior of nanostructured ODS alloys, in: Proceedings of the ICFRM-14 Conference, Sapporo, Japan, 2009.

[35] G. Zhang, Z. Zhou, M. Wang, S. Li, L. Zou, L. Zhang, Tensile and Charpy impact properties of an ODS ferritic/martensitic steel 9Cr-1.8W-0.5Ti-0.35Y_2O_3, Fusion Eng. Des. 89 (2014) 280–283.

[36] M.E. Alam, K. Fields, G.R. Odette, D.T. Hoelzer, S.A. Maloy, Tensile Property Characterization of 14YWT Nanostructured Ferritic Alloy NFA1, Fusion Materials Semiannual Progress Report for Period Ending December 31 (2014), DOE/ER-0313/57, U. S. Department of Energy, 57 (2014) 39-47.

Materials Science & Engineering A 661 (2016) 222–232

Contents lists available at ScienceDirect

Materials Science & Engineering A

journal homepage: www.elsevier.com/locate/msea

Effect of tube processing methods on the texture and grain boundary characteristics of 14YWT nanostructured ferritic alloys

E. Aydogan [a,f,*], S. Pal [b], O. Anderoglu [a], S.A. Maloy [a], S.C. Vogel [a], G.R. Odette [b], J.J. Lewandowski [c], D.T. Hoelzer [d], I.E. Anderson [e], J.R. Rieken [e]

[a] Los Alamos National Laboratory, Los Alamos, NM 87545, USA
[b] University of California, Santa Barbara, Santa Barbara, CA 93106, USA
[c] Case Western Reserve University, Cleveland, OH 44106, USA
[d] Oak Ridge National Laboratory, Oak Ridge, TN 37831, USA
[e] Ames Laboratory, Ames, IA 50011, USA
[f] Texas A&M University, College Station, TX, 77840, USA

ARTICLE INFO

Article history:
Received 15 January 2016
Received in revised form
25 February 2016
Accepted 28 February 2016
Available online 8 March 2016

Keywords:
Texture
EBSD
Neutron diffraction
Nanostructured ferritic alloys

ABSTRACT

Texture and microstructure of tubes and plates fabricated from a nanostructured ferritic alloy (14YWT), produced either by spray forming followed by hydrostatic extrusion (Process I) or hot extrusion and cross-rolling a plate followed by hydrostatic tube extrusion (Process II) have been characterized in terms of their effects on texture and grain boundary character. Hydrostatic extrusion results in a combination of plane strain and shear deformations which generate low intensity α- and γ-fiber components of $\{001\}<110>$ and $\{111\}<110>$ together with a weak ζ-fiber component of $\{011\}<211>$ and $\{011\}<011>$. In contrast, multi-step plane strain deformation by hot extrusion and cross-rolling of the plate leads to a strong texture component of $\{001\}<110>$ together with a weaker $\{111\}<112>$ component. Although the total strains are similar, shear dominated deformation leads to much lower texture indexes compared to plane strain deformations. Further, the texture intensity decreases after hydrostatic extrusion of the alloy plate formed by plane strain deformation, due to a lower number of activated slip systems during shear dominated deformation. Notably, hot extruded and cross-rolled plate subjected to plane strain deformation to ~50% engineering strain creates only a modest population of low angle grain boundaries, compared to the much larger population observed following the combination of plane strain and shear deformation of ~44% engineering strain resulting from subsequent hydrostatic extrusion.

Published by Elsevier B.V.

1. Introduction

Nanostructured ferritic alloys (NFAs) are leading candidates for structural components in nuclear reactors due to their exceptional irradiation tolerance, high strength and resistance to oxidation/corrosion under extreme conditions of temperature and stress [1–6]. There has been substantial progress on optimizing the production of larger heats of NFAs consolidated by hot extrusion (HE), and in some cases, hot isostatic pressing (HIP) [7]. Recently, an NFA with an approximately uniformly distributed population, $\sim 7 \times 10^{23}$ m^{-3}, of ~2.5 nm Y-Ti-O rich nano-oxides (NOs) has been developed by Los Alamos National Laboratory (LANL), Oak Ridge National Laboratory (ORNL) and University of California Santa Barbara (UCSB) in collaboration [8]. The presence of coarsening resistant NOs, along with predominantly fine grain size (< 1 μm) and high dislocation densities imbue NFAs with higher strength and remarkable thermal stability compared to conventional ODS alloys. Moreover, the NOs help to recombine displacement damage and trap neutron irradiation transmutation product, He, in extremely small bubbles, thereby supressing void swelling and grain boundary embrittlement [2,4,9,10].

Although significant progress has been made, some major issues associated with HE NFAs include: severe texturing (the distribution of grain orientations) as well as anisotropic microstructures and properties; and, bimodal grain size distributions [11–19]. The primary detrimental consequences of these characteristics include low fracture toughness and low creep strength in directions parallel to, and transverse to the HE axis, respectively [3,7,12,19–22]. Additional deformation processing steps to improve properties and/or fabricate shapes are also severely impacted by these characteristics of the HE condition. For example, HE cross-rolled plates develop microcracks [23] and deformation

* Corresponding author.
E-mail address: aydogan@lanl.gov (E. Aydogan).

http://dx.doi.org/10.1016/j.msea.2016.02.085
0921-5093/Published by Elsevier B.V.

processed tubes experience radial through-wall cracks [24]. Extensive research in Japan and France have identified semi-optimized processing paths for tubing that differ in detail, but in both cases involve a series of cold-pilgering steps to reduce the wall thickness, with intermediate and final heat treatment softening schedules [5,25,26]. This general processing path has been most successful with lower 9Cr transformable steels [7], but 14YWT ferritic stainless NO strengthened alloys remain difficult to process into thin-walled tubing.

Recent studies have suggested that material with low ductility can effectively be processed to a near net shape using hydrostatic extrusion. It can also produce the final product with enhanced and more isotropic mechanical properties, as well as high powder consolidation densities [27–29]. For example, a recent review [30], and related research on hydrostatically extruded NiAl [31], revealed improved properties and beneficial changes in texture [32] due to the shear dominated stress state generated in hydrostatic extrusion. One hydrostatic extrusion path uses a high-pressure fluid in a die chamber to impose compressive stresses that lower ram pressures and temperatures, resulting in better formability and surface finishes [30–33].

In this study, the effects of different processing routes on texture and grain boundary characteristics of as processed 14YWT NFA tubes have been investigated using neutron and electron diffraction techniques.

2. Experimental procedures

The composition of the NFA tested in this study is 12.8 wt%Cr-2.95W-0.38Ti-0.22Y-Fe for both tubes. In order to understand the effects of different processing methods on the resulting texture and grain boundary characteristics, 14YWT tubes were produced by two different initial routes followed by a novel hydrostatic extrusion process to produce tubes that were processed to full density. Process I utilizes the initial processing method of thermal spraying while Process II uses a conventional mechanical alloying method followed by hot extrusion. Fig. 1 shows that Process I is the combination of gas atomization reaction synthesis of Fe-based NFA precursor powders, deposited by high velocity oxy-fuel (HVOF) thermal spray methods on tubular pre-forms, followed by hydrostatic extrusion to process the tube to final dimensions. A “mother tube” was manufactured through HVOF deposition on an Al mandrel with Fe-based NFA precursor powders (20–53 μm dia.). The fugitive Al mandrel was removed from the deposit section with a phosphoric acid etching treatment and initial machining was performed to remove the interior (~250 μm) layer of intermetallic phase (FeAl or Fe_3Al) that appeared to form during the deposition process. The samples were then heat treated at 1000 °C for 5 h under vacuum following thermal spray deposition to promote the oxygen exchange reaction and Y-Ti-O dispersoid formation within the coating. Finally, hydrostatic extrusion was applied two times with a 4:1 area reduction (~44% engineering strain) at 815 °C by using a solid support mandrel plus external can to create a beneficial stress state for extrusion.

The schematic for Process II is shown in Fig. 2. Powders were first produced by gas atomization method by ATI Powder Metals Laboratory (Pittsburgh, PA). After atomization, the Y phase separates and requires ball milling to create a more homogenous chemistry. So, the nominal 14 wt%Cr-3W-0.35Ti-0.25Y iron alloy powder was ball milled by Zoz, GmbH (Wenden, Germany) with the addition of FeO powder for 40 h in a CM100b attritor mill. The powders were sealed in cans backfilled with Ar to remove any atmosphere contamination and degassed at 400 °C. The canned powders were then hot extruded at 850 °C to create a solid billet. After extrusion, the alloy was annealed for 1 h at 1000 °C and then hot cross-rolled at 1000 °C to a ~50% of thickness reduction (50% engineering strain) resulting in a final thickness of ~10 mm. The solid billet was then electro-discharge machined (EDM) in the direction perpendicular to hot cross-rolling direction to produce a tube. This tube was then hydrostatically extruded at 815 °C using the same process described for the thermally sprayed tube. Fig. 3 shows the tubes with a final wall thickness of 0.5 mm and outer diameters of ~8 mm and ~3.5 mm for Process I and Process II, respectively.

Grain boundary characteristics were investigated by orientation imaging microscopy (OIM) while texture analysis was implemented using both OIM and neutron diffraction methods. OIM by electron backscatter diffraction (EBSD) using a scanning electron microscope (SEM) was used to examine the grain boundary characteristics and texture of the plate and tubes. It should be noted that EBSD is limited to the grain size studies down to 60 nm [34,35]. Here, EBSD was carried out in an FEI Inspect FEG SEM equipped with TSL EBSD detector. All the experiments were performed by tilting the sample at 70° from the horizontal, at an acceleration voltage of 20 kV and aperture size of 50 μm. The sizes of the scanned regions was either 60 μm × 90 μm or 240 μm × 320 μm, where the step size for the data collection was chosen based on the grain and substructure dimensions. Samples for the EBSD scans were obtained from the tube and plate faces that were prepared to achieve very smooth surfaces by standard metallographic techniques followed by jet electropolishing using a solution of perchloric acid (5%) and methanol at −40 °C with an applied voltage of 20 V.

Bulk texture measurements probing the grain orientation distribution function over the complete volume of each sample were collected on the HIPPO instrument at the pulsed neutron spallation source at LANSCE [36]. The samples were located ~9 m from the neutron moderator and diffracted neutrons were detected by 1240 ^{3}He tubes arranged on panels distributed over five conical rings with scattering angles ranging from $2\theta = 40–150°$. Samples were glued on standard HIPPO holders, with their tube axis parallel to the holder axis, and then loaded into the robotic sample-changer. The entire ~10 mm long tubes were centered in a 10 mm diameter beam, thus capturing the entire sample volume. Diffraction patterns were collected over ~20 min for samples rotated around the vertical axis at 0, 67.5 and 90°. The diffraction data was analyzed by simultaneous Rietveld analysis of 135 diffraction patterns using the E-WIMV texture algorithm with a 10° resolution of the orientation distribution function.

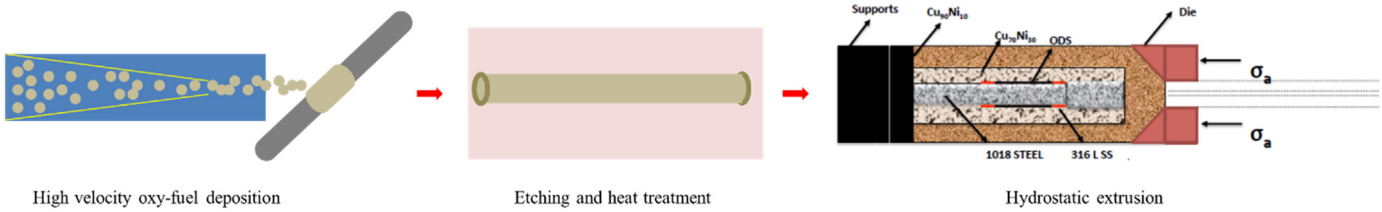

Fig. 1. Processing steps of Process I.

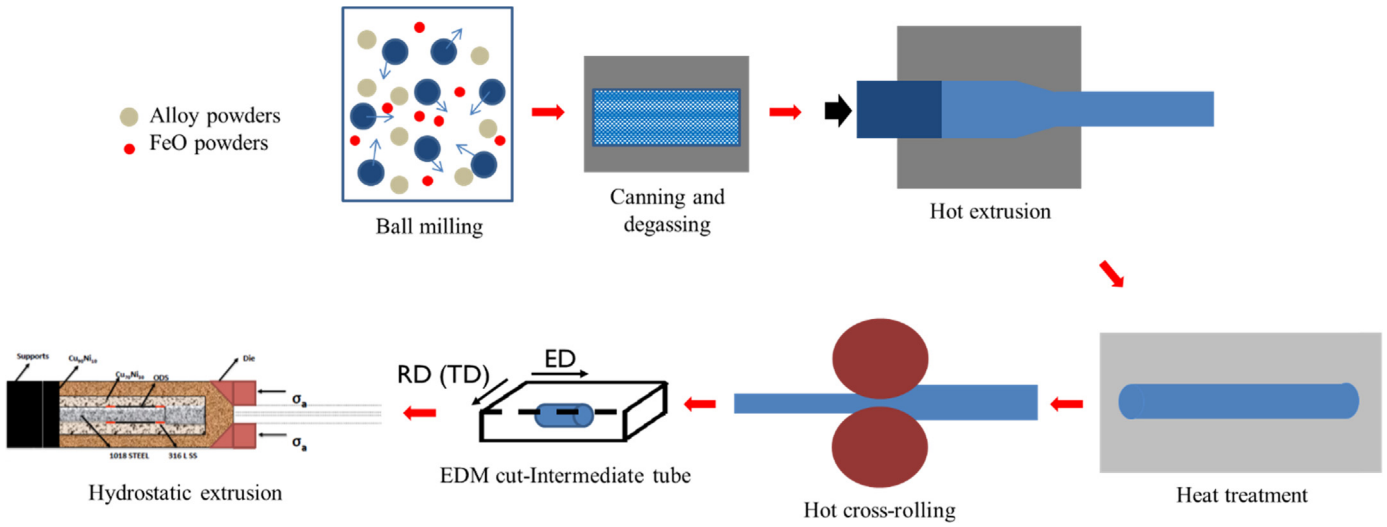

Fig. 2. Processing steps of Process II (RD: rolling direction, TD: transverse direction, ED: extrusion direction).

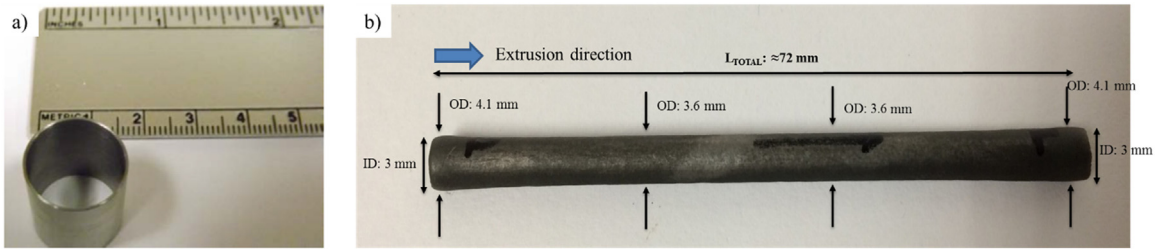

Fig. 3. Photos showing the final dimensions of the tubes produced by: a) Process I, and b) Process II.

Orientation distribution function (ODF) analysis and pole figure plotting for both electron and neutron texture measurements were performed using the MTEX package [37]. The EBSD data was analyzed using the TSL OIM Analysis 7 software.

3. Results

3.1. Tube processing by Process I

The only deformation that occurs in consolidation by Process I is by hydrostatic extrusion and the corresponding microstructures isolate the unique effects of this processing path. Fig. 4a shows the orientation distribution of the grains obtained by the OIM analysis of the 14YWT sample produced by Process I. Even though the physical extrusion direction is shown in a diagonal direction in the map, the coordinates of the map have been rotated in such a way that the extrusion direction is into the page in order to determine the grain orientations in the extrusion direction. Consequently, predominantly existing green color infers that most of the grains are oriented with a (101) plane normal that is parallel to the extrusion direction. The band contrast map in Fig. 4b together with Fig. 4c show that Process I results in wide grain area fraction distribution as a function of size. However, there are many more small grains that yield a corresponding average diameter of ~2 μm. Fig. 4d shows that hydrostatic extrusion results in a large fraction (~53%) of low angle boundaries (LABs) with misorientation angles between $2° < \theta < 15°$.

Fig. 5 shows the pole figures of the sample produced by Process I as determined by both neutron diffraction (Fig. 5a) and EBSD (Fig. 5b). Even though data processing functions and probed sample volumes are greatly different for neutron diffraction and EBSD, both produce similar pole figures with only a slight difference in the texture intensity. From the pole figures it is obvious that the hydrostatic extrusion to 44% strain produces a typical α-fiber texture $<110>\parallel$ED, generally common to deformation processed ferritic alloys [38,39].

The ideal orientations of texture components in bcc materials are shown schematically for $\varphi_2=0°$ and 45° ODF sections in Fig. 6 and Table 1 [40]. For bcc steels, the important fiber textures are the α-fiber ($<110>\parallel$RD), ε-fiber ($<011>\parallel$TD), γ-fiber ($<111>\parallel$ND), η-fiber ($<100>\parallel$RD), θ-fiber ($<001>\parallel$ND), and ζ-fiber ($<011>\parallel$ND) [41,42] where RD, TD and ND stand for rolling direction, transverse direction and normal direction, respectively. It should be noted that 'RD' will be replaced by 'ED' throughout the paper.

Although EBSD might not give fully representative results because of its limited probed volume, Fig. 5 confirms that the probed area on the tube surface using OIM analysis represents the bulk texture obtained by neutron diffraction well. However, there might be a texture gradient through the thickness of the tube wall. In order to further examine and represent the bulk texture, detailed analyses of ODF plots and inverse pole figures were obtained using the neutron diffraction method. It is worthwhile to point out that while neutron diffraction probes a much larger volume than OIM, all spatial information is lost. Hence, while the detailed texture analyses were employed using neutron diffraction, only OIM can provide grain misorientation angles and orientation maps.

Fig. 7 shows the neutron diffraction resulted ODF maps for the 14YWT sample produced by Process I at constant $\varphi_2=0°$ and $\varphi_2=45°$. Comparing these maps with Fig. 6 shows that the dominant texture is α-fiber at $<110>$ having the strongest intensity on $\{001\}<110>$. Furthermore, weaker γ-fiber component of $\{111\}<110>$ and ζ-fiber on $\{011\}<211>$ and $\{011\}<011>$ can be observed. The overall texture index was calculated as 2.6 using ODF neutron diffraction data indicating a moderate

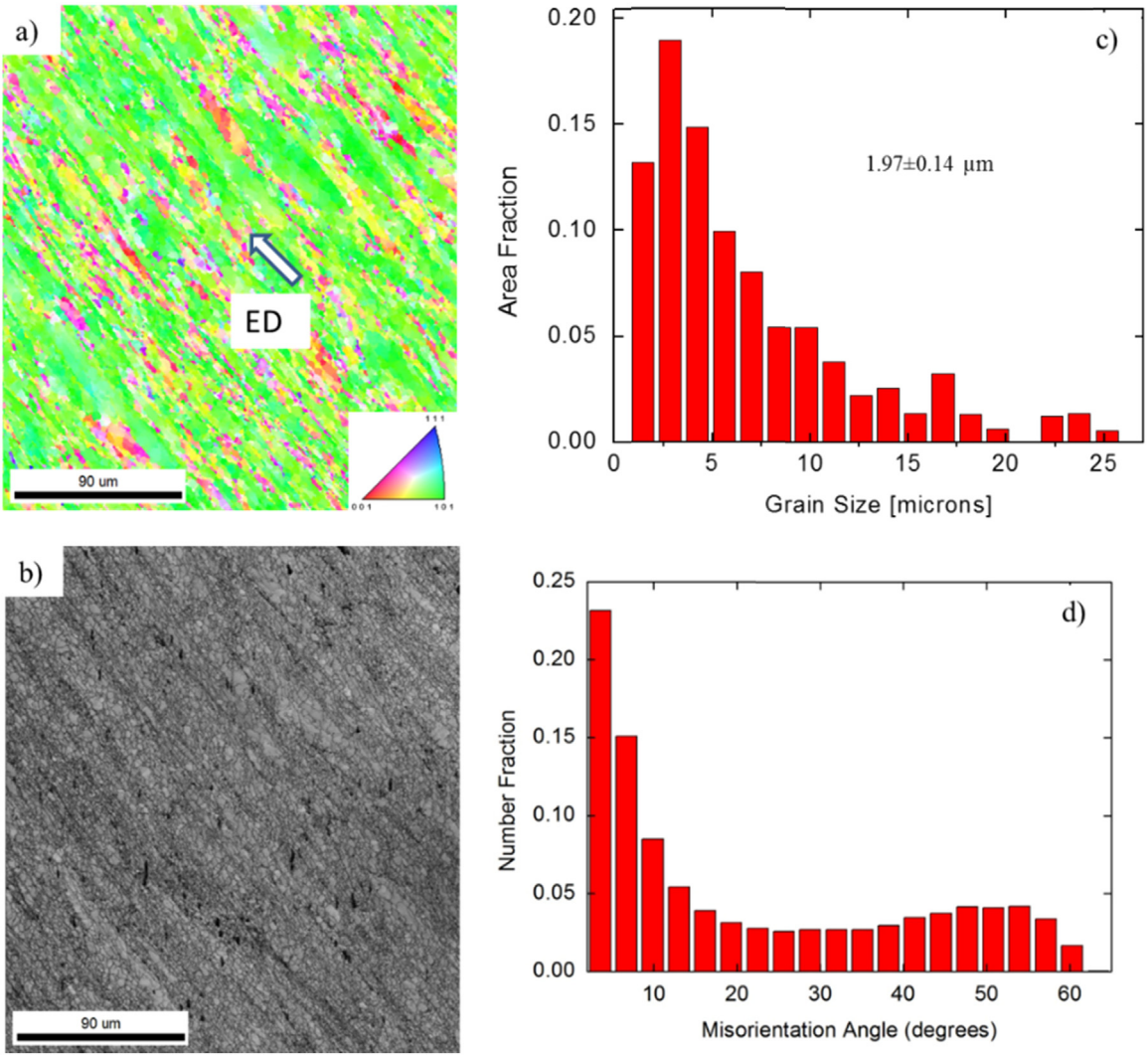

Fig. 4. An OIM showing a) the crystallographic orientation of the grains; b) the corresponding band contrast gray scale map of the grain structure; c) the grain area distribution as a function of the grain size; and, d) the grain boundary misorientation angle distribution in 14YWT samples produced by Process I. (For interpretation of the references to color in this figure, the reader is referred to the web version of this article.)

texture strength relative to a texture index of 1 for a perfectly random texture and infinity for a single crystal.

3.2. Tube processing by Process II

Fig. 8 shows EBSD measurements on the 14YWT intermediate tube, EDM-cut from the hot extruded and cross-rolled plate, with information analogous to that shown in Fig. 4 for the tube, only hydrostatically extruded in Process I. Note the tube is microstructurally identical to the cross-rolled plate, differing only in its geometric reference orientation. Since this alloy condition was characterized before the final hydrostatic extrusion step, as illustrated in Fig. 2, it is designated as being "intermediate". Fig. 8a is an orientation distribution map. The arrows indicate the initial hot extrusion (ED) and the transverse cross-rolling directions (RD). The predominantly red color infers that most of the grains are oriented with (100) plane normal parallel to the tube wall thickness. Fig. 8b–d show that the intermediate tube has a tri-modal grain size distribution and fewer LABs (~32%) compared to the tube produced by Process I (53%).

Since the intermediate tube was cut from the cross-rolled plate, the coordinates of the plate were transformed into the tube coordinates as shown in Fig. 9. There is a common extrusion direction (ED) for the plate and tube. Radial wall thickness directions of the tube are designated ThD and directions corresponding to the normal and rolling directions are designated as ThND and ThRD, respectively. However, the tube surface ED is only parallel to that for the plate surface at 0° and 180° around the circumference, while it is parallel to the plate sides at 90° and 270°.

Fig. 10 shows the pole figures of the intermediate tube determined by both neutron diffraction (Fig. 10a) and EBSD (Fig. 10b) at 0° (or 180°). The pole figures calculated by both methods are again similar, with slight intensity differences observed. Based on the coordinate system defined above, pole figures indicate that the intermediate tube has texture of both $<110>\|$ThRD and $<200>\|$ThND. Moreover, as it must, the intermediate tube RD shares the $<110>$ α-fiber texture with the cross-rolled plate. As discussed elsewhere [24], (100)-type planes lie parallel to the plate faces as well as to the tube surface at 0° and 180°, while they are normal to the tube surface at 90° and 270° as illustrated in Fig. 9. The $\{001\}<110>$ system is oriented for brittle cleavage fracture leading to microcracking in the plate [24] and radial tubing cracks, especially at 90° and 270°. The intermediate tube has a strong neutron diffraction texture index of 10.1.

Fig. 11 shows the sections of the neutron diffraction resulted ODF maps in Euler space for the intermediate 14YWT tube at

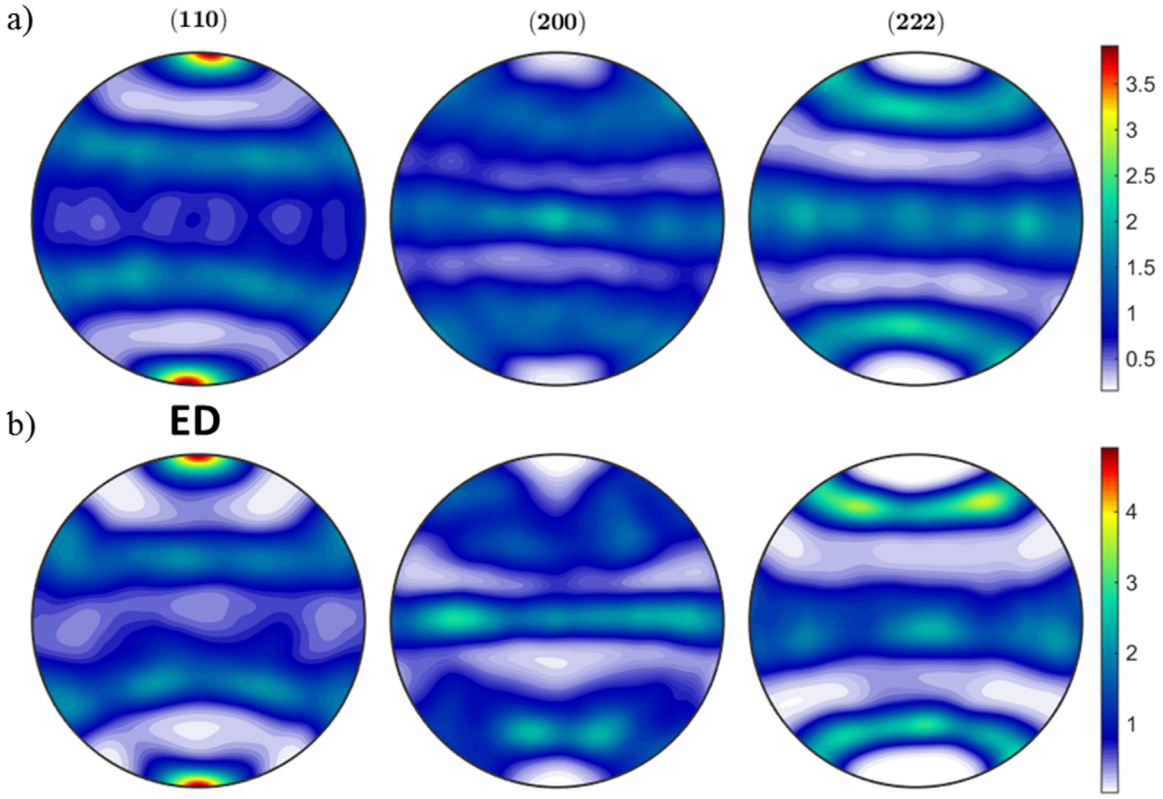

Fig. 5. Pole figures of 14YWT samples produced by Process I and obtained by a) neutron diffraction and b) EBSD techniques. (ED: extrusion direction). (For interpretation of the references to color in this figure, the reader is referred to the web version of this article.)

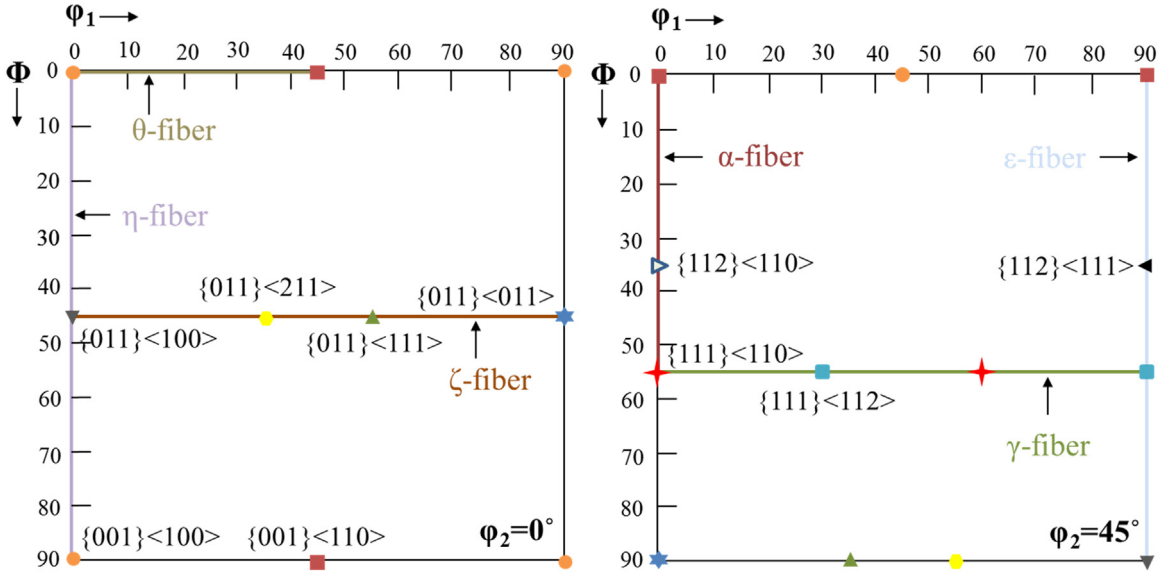

Fig. 6. Schematic illustration of the important texture components in bcc materials (*Reproduced from Ref.* [40]). (For interpretation of the references to color in this figure, the reader is referred to the web version of this article.)

Table 1
Important fiber textures and orientations for bcc materials [40].

Fiber name	Fiber axis	Components
α	$<110>\|\|RD$	$\{001\}<110>$, $\{112\}<110>$, $\{111\}<110>$
ε	$<011>\|\|TD$	$\{001\}<110>$, $\{112\}<111>$, $\{111\}<112>$, $\{011\}<100>$
γ	$<111>\|\|ND$	$\{111\}<110>$, $\{111\}<112>$
η	$<100>\|\|RD$	$\{001\}<100>$, $\{011\}<100>$
θ	$<001>\|\|ND$	$\{001\}<100>$, $\{001\}<110>$
ζ	$<011>\|\|ND$	$\{011\}<100>$, $\{011\}<211>$, $\{011\}<111>$, $\{011\}<011>$

constant $\varphi_2=0°$ and $\varphi_2=45°$. When compared with Fig. 6, it can be seen that intermediate tube has strong θ- and ε-fiber on $\{001\}<110>$ together with a weak γ-fiber on $\{111\}<112>$. It should be noted that the main deformation axis is considered as the axis for all tubes, which is the extrusion direction. However, as shown in Fig. 10, intermediate tube has a stronger texture in rolling direction through the wall thickness (at 90° and 270°), which is transverse to the extrusion direction. Since the rolling direction was taken as the transverse direction during ODF calculations, the corresponding plots of the intermediate tube, by

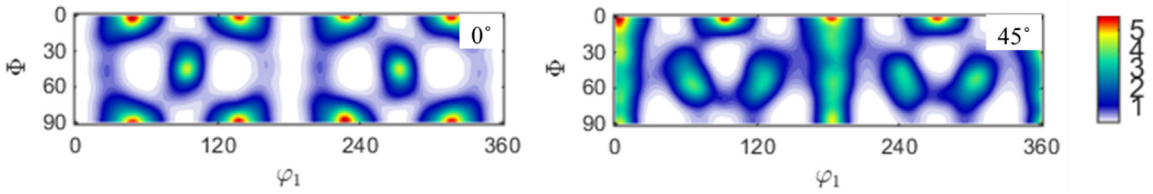

Fig. 7. The neutron diffraction produced ODF, represented as sections in Euler space, for the 14YWT tube produced by Process I at φ_2 values of 0° and 45°. (For interpretation of the references to color in this figure, the reader is referred to the web version of this article.)

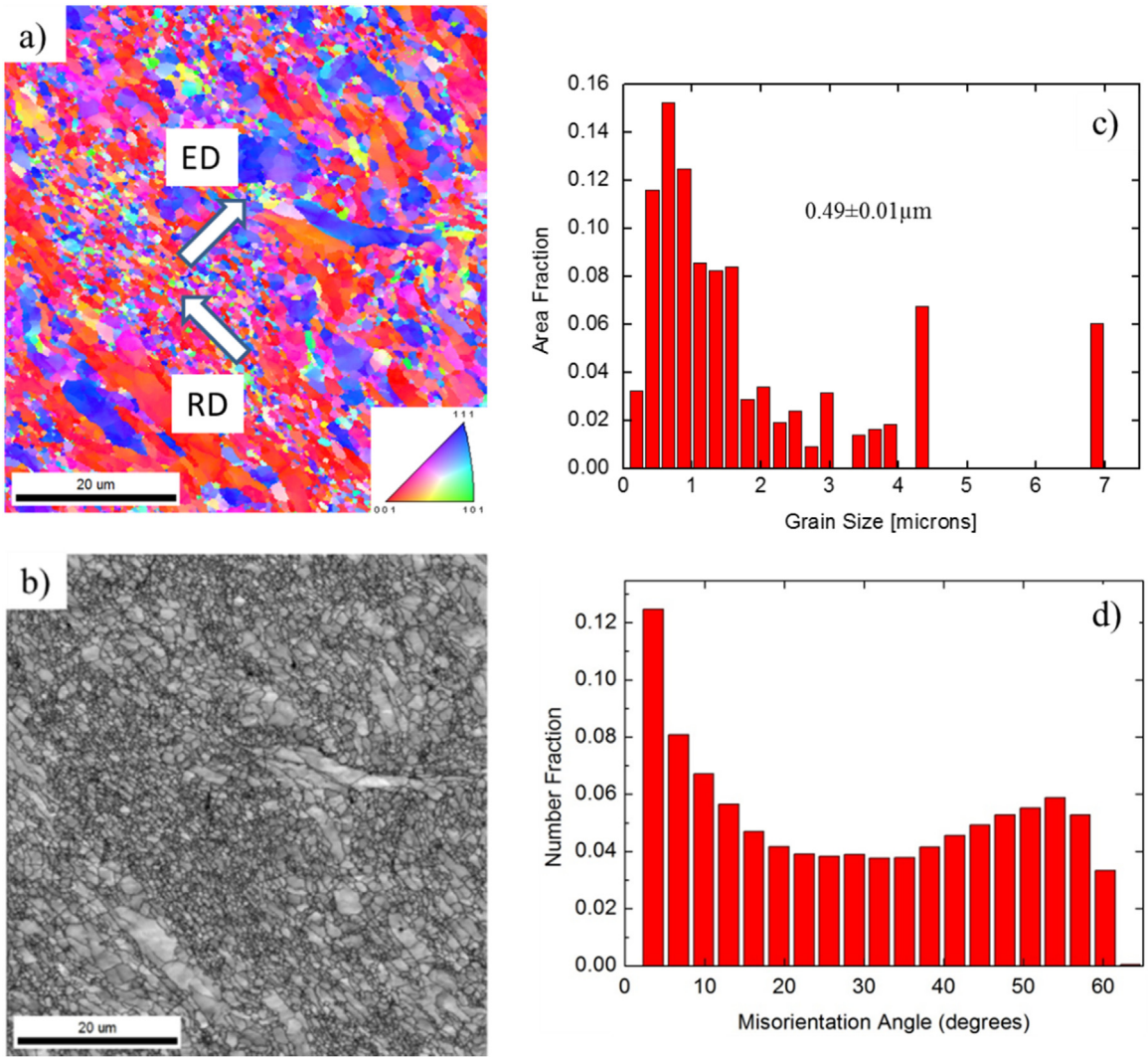

Fig. 8. EBSD characterization of the intermediate tube showing a) an orientation map of the crystallographic distribution of the grains; b) a band contrast map of the grain structure in gray scale; c) the grain area distribution as a function of size; and, d) the grain boundary misorientation angle distribution. (For interpretation of the references to color in this figure, the reader is referred to the web version of this article.)

reference frame definition, exhibit θ- and ε-fiber texture ($<110>\|$TD) rather than α-fiber ($<110>\|$RD) which is a typical texture for ferritic steels, as found in the plate. Again, the actual microstructures are identical in both cases.

Fig. 12a shows the orientation map of the grains in the extracted tube after final hydrostatic extrusion as described in Fig. 2. The coordinates of the map have been rotated in such a way that the radial direction of the tube (normal direction-ND) points through the page. Consequently, the predominantly existing red color infers that most of the grains are oriented with (100) plane normal parallel to the sample normal direction. The band contrast map in Fig. 12b and grain size plot in Fig. 12c show that very small and very large grains exist, suggesting a bimodal grain size distribution with an average grain size of ~0.5 μm. Fig. 12d shows that fraction of LABs increases from 32% to 46% after hydrostatic extrusion.

Fig. 13 shows the pole figures of the tube after hydrostatic extrusion derived by both neutron diffraction (Fig. 13a) and EBSD (Fig. 13b), yielding different results in this case. While the neutron diffraction indicates a broken fiber texture of $<110>\|$ED, both the EBSD orientation map and pole figures show a maximum texture index in $<200>\|$ND. However, the difference between the bulk texture obtained by neutron diffraction and surface texture determined by EBSD is the result of the position of the EBSD sample on the SEM stage. Since the data shows the maximum texture on $<200>$ rather than $<110>$, the EBSD reflects a

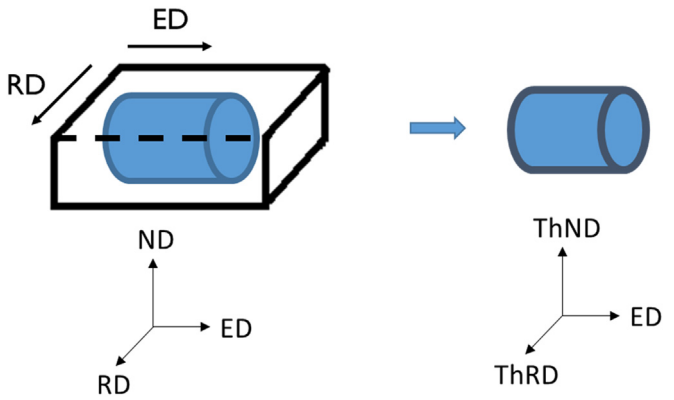

Fig. 9. Coordinate system of the intermediate tube transformed from the plate form.

region that is aligned 45° to the extrusion direction. Since the samples are tubes, their orientation reference frame determines the nominal texture that must be considered in reaching any conclusions or in making comparisons.

The neutron diffraction data shows that the initial processing steps of hot extrusion, annealing and hot cross-rolling, leads to discontinuity in the fiber texture as shown in Fig. 13a. The overall texture index was calculated as 8.6 using neutron diffraction. The texture index decreased from 10.1 to 8.6 after hydrostatic extrusion with 25% strain in the intermediate tube, since the principal deformation direction is in the opposite to that for the hot cross-rolling. These results in combination with those observed for Process I, indicate that hydrostatic extrusion produces relatively weak textures.

Fig. 14 shows the neutron diffraction resulted ODF maps of the 14YWT final tube produced by Process II at constant $\varphi_2=0°$ and $\varphi_2=45°$. If they are compared with Fig. 6, it can be seen that α-fiber has the maximum intensity on $\{111\}<110>$ along with a weak discontinuous γ-fiber on $\{001\}<110>$. For $\varphi_2=0°$ there is a very weak ζ-fiber texture on $\{011\}<211>$ and $\{011\}<011>$.

4. Discussion

Large-scale deformation behavior of polycrystalline Fe is quite complex since it activates a number of different slip planes like {110}, {112} and {123}, and unlike fcc materials, is not confined to only closed packed planes. Depending upon various factors like mode of deformation, processing history (strain path), composition, initial microstructure and orientation of the grains, deformation involves different combinations of these slip systems. These multiple factors also affect the dislocation substructure and local misorientations between sub-grains. The result is the production of a wide range of possible textures in the final microstructure [43]. In the present study two different large deformation processing methods were used to fabricate tubes. Both Process I and II create microstructures with a strong $<110>\|ED$ texture with various grain sizes.

Rolling and extrusion are usually regarded as plane strain deformations. However, a gradient in the stress state exists in the through thickness of a rolled or extruded plate. Deformation in the near surface region, in contact with the die, is dominated by a shear component. The center of the plate experiences compressive stresses and deformation occurs under plane strain conditions [44]. In contrast, during hydrostatic extrusion of a thin-walled tube the outer layer is dominated by a state of compressive stress, while the central layer is deformed by a dominant shear stress component [45].

It is observed that both hydrostatic extrusion and conventional hot extrusion processes produce a strong texture on $\{001\}<110>$; however, there are remarkable differences in the texture intensities. The tube produced through hydrostatic extrusion in Process I shows maximum texture index of 2.6, whereas the tube produced at the intermediate step in Process II which experienced a similar amount of deformation shows a much

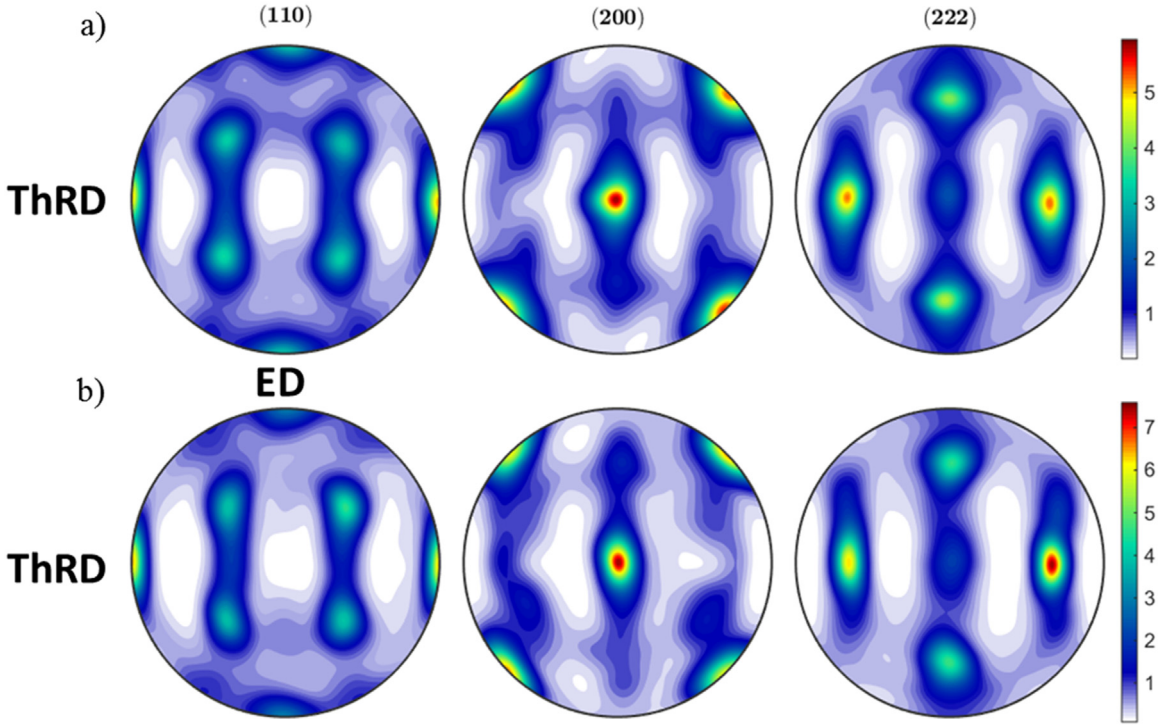

Fig. 10. Pole figures of intermediate 14YWT tube obtained by: a) neutron diffraction, and b) EBSD techniques. (For interpretation of the references to color in this figure, the reader is referred to the web version of this article.)

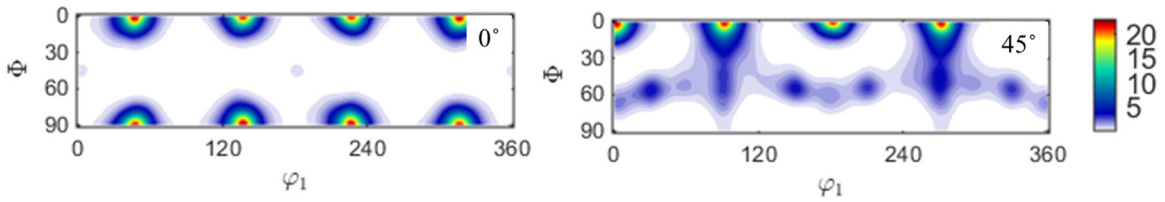

Fig. 11. ODF, represented as sections through Euler space, of the intermediate 14YWT tube at constant φ_2 values of 0° and 45°. (For interpretation of the references to color in this figure, the reader is referred to the web version of this article.)

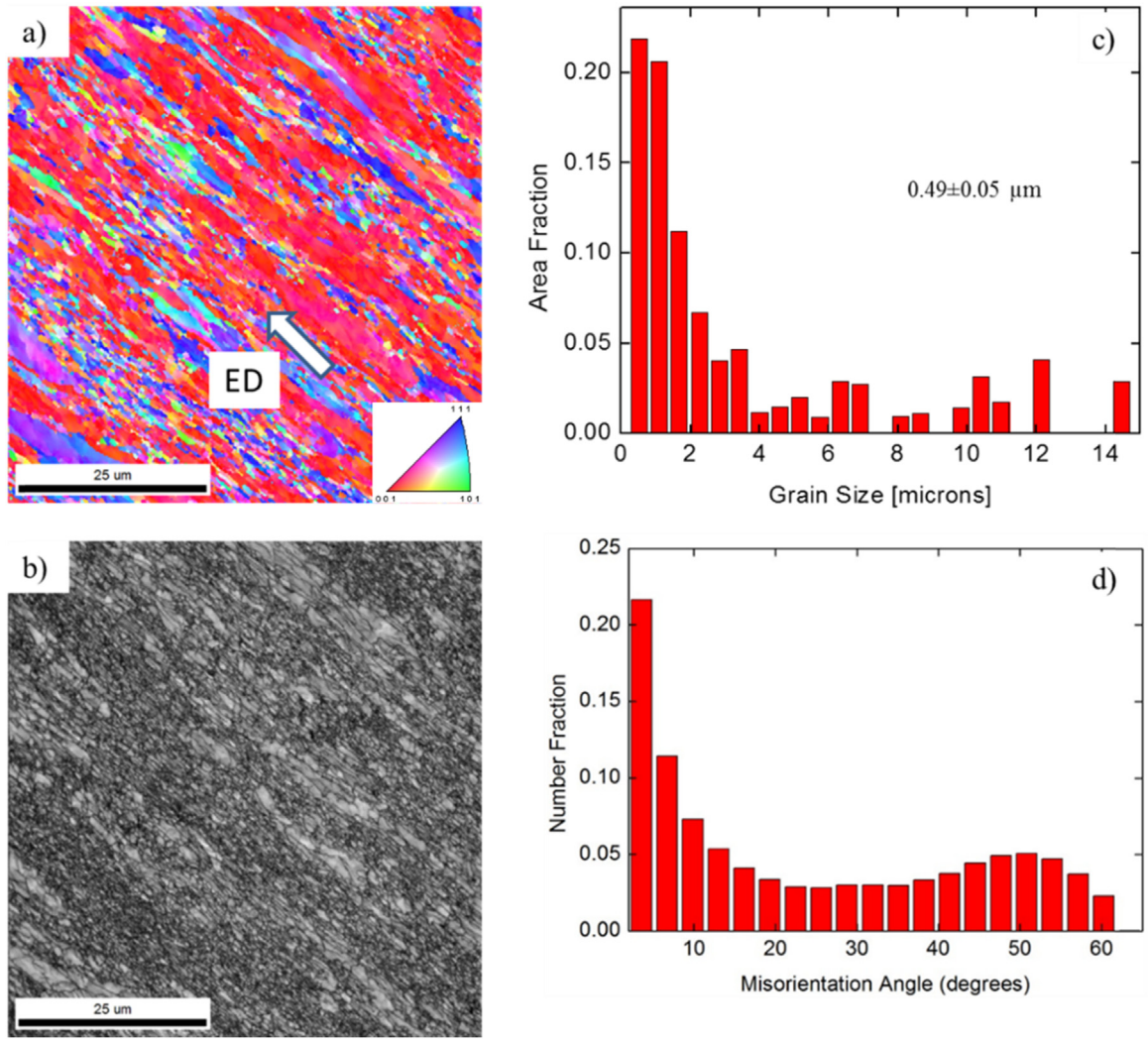

Fig. 12. a) Orientation map showing the crystallographic distribution of the grains; b) band contrast map showing the microstructure in gray scale; c) grain size distribution plot; and, d) grain boundary misorientation angle distribution in 14YWT final tube produced by Process II. (For interpretation of the references to color in this figure, the reader is referred to the web version of this article.)

stronger texture index of 10.1. Pal et al. [24] has investigated the inverse pole figures of the Process II produced intermediate plate before EDM cutting tubes from it as well as after hydrostatically extruding the intermediate tube. The texturing found here is generally consistent with their study; while the textures in the plate and the hydrostatically extruded tube are similar in the extrusion direction, the maximum texture intensity changes from $<100>$ to $<111>$ in the tube thickness normal direction as a result of the hydrostatic extrusion. This rationalizes the observation that while the intermediate plate exhibits an extensive amount of microcracking, the hydrostatically extruded final tube with a texture on $<111>$||ND resists such cracking in Process II [24]. Similarly, comparing the inverse pole figures of the hydrostatically extruded final and intermediate tubes shown in Fig. 15 reveals that while hydrostatic extrusion develops a texture of a mixture of $<111>$ and $<100>$ along the ND, $<100>$ is more profound along the ND of the intermediate tube. Hot working of the bcc steels results in cold rolling textures if the material does not undergo any kind of ferrite to austenite transformation or complete recrystallization [44,46]. Since 14YWT steels are fully ferritic and do not recrystallize during the present hot-working conditions, the observed texture differences can be explained in terms of cold rolling textures. Raphanel et al. [47] predicted the cold rolling texture of bcc steel based on a relaxed constant

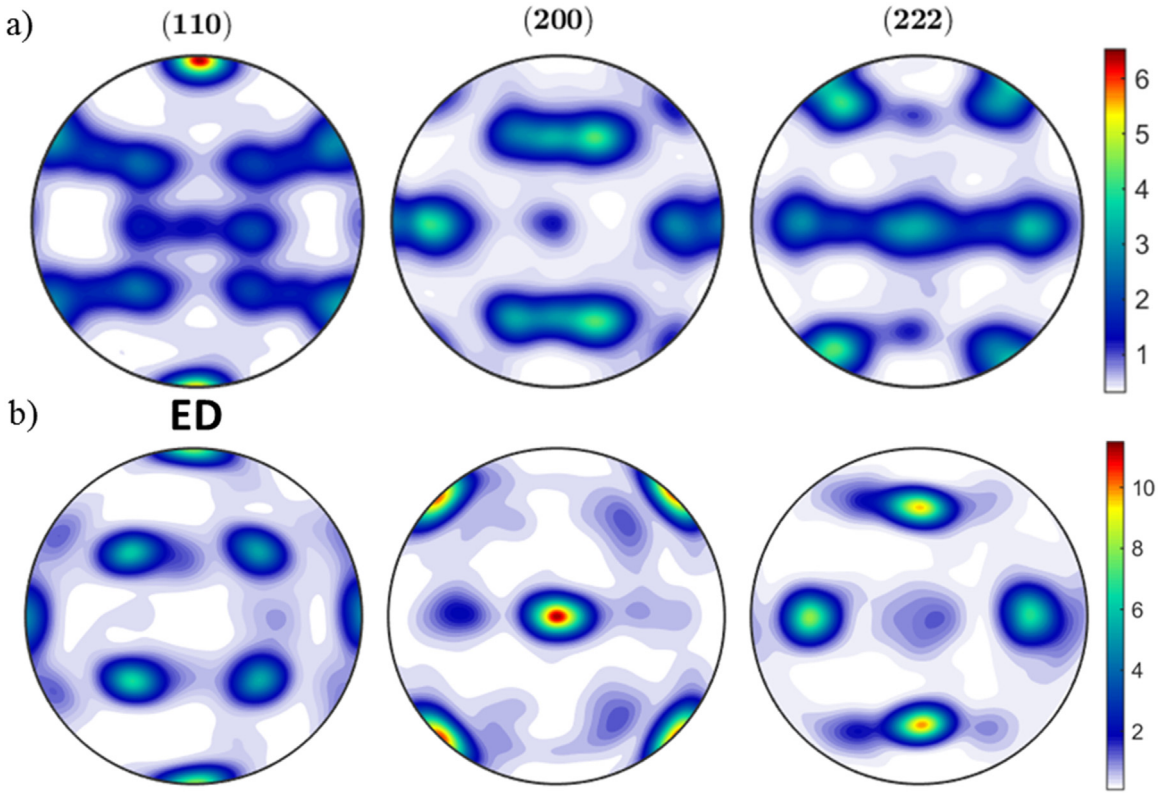

Fig. 13. Pole figures of 14YWT final tube after hydrostatic extrusion obtained by: a) neutron diffraction, and b) EBSD techniques. (For interpretation of the references to color in this figure, the reader is referred to the web version of this article.)

modification of Taylor theory. Simulations by reducing ε_{13} and ε_{23} shear strain components increases the intensity of $\{001\}<110>$ texture and produces an elongated pan-cake shaped grains, as was observed in the cross-rolled plate and intermediate tube. Consequently, formation of high volume fraction of $\{001\}<110>$ texture components in the intermediate tube orients the {001} plane normal along the tube thickness normal direction (shown in Fig. 15b).

Our results show that after hydrostatic extrusion of the intermediate tube in Process II, the texture index is weakened from 10.1 to 8.6. Raabe [48] also reported that the shear stress weakens the texture relative to the pre-deformed condition. This is simply attributed to a lower number of activated slip systems during pure shear deformation. The major texture component originating under simple shear deformation of a bcc steel is the 'Goss' texture component $\{110\}<001>$. However, the 'Goss' texture component is not very stable, and can easily transform to the stable components of $\{001\}<110>$ of α-fiber or $\{111\}<110>$ of γ-fiber depending upon the relative strength of each fiber [48]. This is responsible for the origin of weak shear texture components of $\{111\}<110>$ and $\{001\}<110>$ producing a partial $<111>\|ND$ texture.

The compressive part of the stress in hydrostatically extruded tubes introduces the common α-fiber. The nature of the deformation process is further corroborated using the number fraction vs. misorientation angle plots in Fig. 16. The hydrostatically extruded tubes contain large fraction of LABs indicating the association of shear deformation and high amount of local reorientation [43], which in turn produces a continuous spread of orientation along α-fibers rather than developing a sharp texture. The effect of hydrostatic extrusion is more drastic when the starting material possesses a pre-existing texture (due to hot cross-rolling and extrusion), completely changing the texture. In this case, the maximum texture intensity is observed on the $\{111\}<110>$ component of γfiber due to the restriction of activated slip system and activation of high Taylor factor shear planes. Development of strong γ-fiber has been reported to be good for deep drawing form ability of high chrome ferritic steels [48]. It also supports the finding that the hydrostatically extruded final tube in Process II can be produced without cracking as reported by Pal et al. [24].

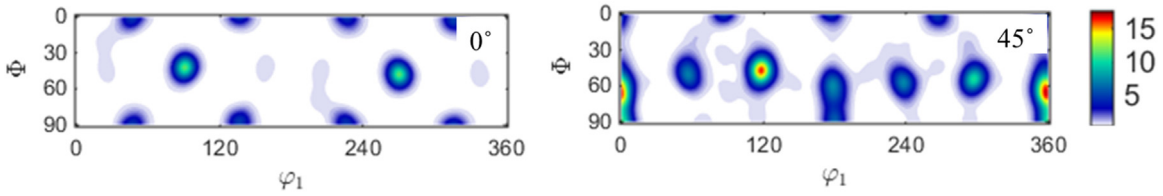

Fig. 14. ODF, represented as sections through Euler space, of the 14YWT final tube after hydrostatic extrusion at constant φ_2 values of 0° and 45°. (For interpretation of the references to color in this figure, the reader is referred to the web version of this article.)

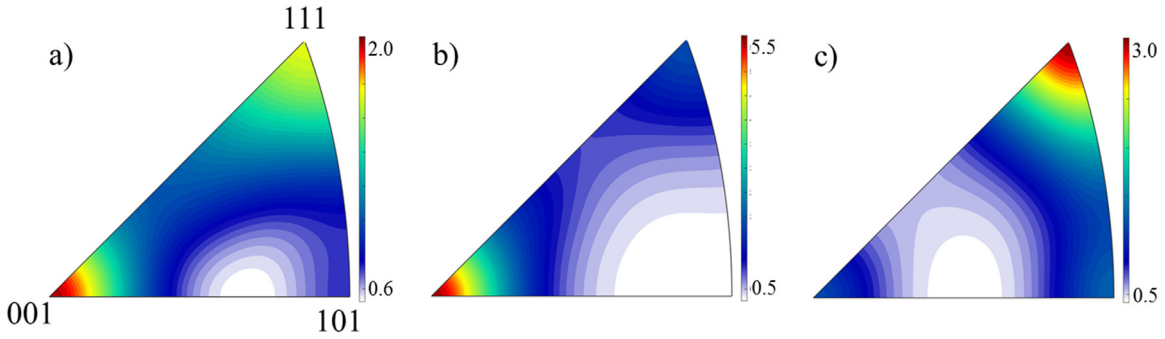

Fig. 15. Neutron diffraction produced inverse pole figures of a) hydrostatically extruded final tube in Process I, b) intermediate tube in Process II and c) hydrostatically extruded final tube in Process II. (For interpretation of the references to color in this figure, the reader is referred to the web version of this article.)

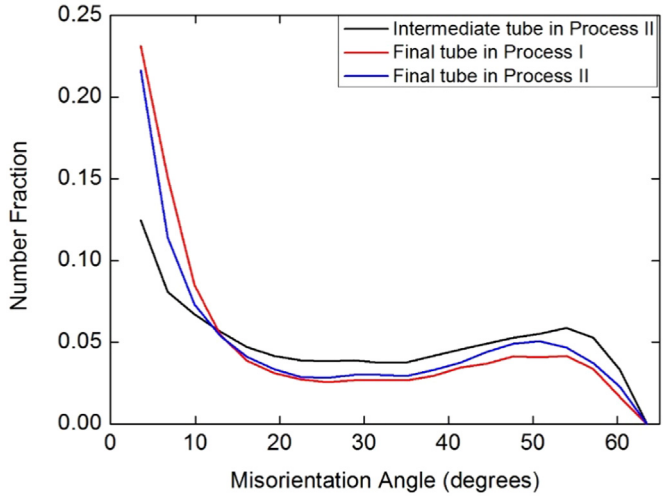

Fig. 16. Grain boundary misorientation angle distribution of three different tubes produced by Process I and II. (For interpretation of the references to color in this figure, the reader is referred to the web version of this article.)

5. Conclusions

In this study, the effect of different processing routes on texture and grain boundary characteristics for 14YWT NFA tubes have been investigated. Hydrostatic extrusion which introduces a combination of plane strain and shear deformations results in α- and γ-fibers on $\{001\}<110>$ and $\{111\}<110>$ as well as weak textures of ζ-fiber on $\{011\}<211>$ and $\{011\}<011>$. On the other hand, hot extrusion and cross-rolling processes result in plane strain deformations in the case of intermediate plate and tube in Process II, leading to a strong texture on $\{001\}<110>$ together with weak texture on $\{111\}<112>$. While both conventional hot extrusion and innovative hydrostatic extrusion produce a pronounced texture on $\{001\}<110>$, shear deformation introduced during hydrostatic deformation produces $<111>\|ND$ texture component. Furthermore, hydrostatic extrusion results in weaker textures compared to the hot extrusion and rolling textures. Even though the final tube produced by Process I and the intermediate tube in Process II are exposed to similar amounts of deformation, the former has a texture index of 2.6 while the latter has a texture index of 10.1. Similarly, when the intermediate tube is hydrostatically extruded, its texture index decreases to 8.6. Together with a decrease in the texture index, α-fiber on $\{001\}<110>$ weakens and γ-fiber on higher Taylor factor planes, $\{111\}<110>$, strengthens as a result of a reduced number of activated slip systems during shear deformation. Moreover, the effect of hydrostatic extrusion on the grain boundary characteristics is quite strong. Local reorientation during shear deformation results in high fractions of LABs compared to the intermediate tube produced by plane strain deformation.

Acknowledgements

This research was partially supported by DOE-NE Fuel Cycle Research and Development Program under the Contract number DE-AC52-06NA25396.

References

[1] R.L. Klueh, D.J. Alexander, J. Nucl. Mater. 233–237 (1996) 336–341.
[2] G.R. Odette, M.J. Alinger, B.D. Wirth, Ann. Rev. Mater. Res. 38 (2008) 471–503.
[3] S. Ukai, S. Ohtsuka, Energy Mater. 2 (2007) 26–35.
[4] G.R. Odette, D.T. Hoelzer, JOM 62 (9) (2010) 84–92.
[5] S. Ukai, Comprehensive Nuclear Materials, Elsevier B.V., Germany, 2012, Ch. 4.08.
[6] G.R. Odette, JOM 66 (12) (2014) 2427–2441.
[7] S.M. Ukai, M. Fujiwara, J. Nucl. Mater. 307–311 (2002) 749–757.
[8] N.J. Cunningham, Y. Wu, A. Etienne, E.M. Haney, G.R. Odette, et al., J. Nucl. Mater. 444 (2014) 35–38.
[9] T. Yamamoto, G.R. Odette, P. Miao, D.J. Edwards, R.J. Kurtz, J. Nucl. Mater. 386–388 (2009) 338–341.
[10] G.R. Odette, P. Miao, D.J. Edwards, J. Nucl. Mater. 417 (2011) 1001–1004.
[11] M.K. Miller, D.T. Hoelzer, E.A. Kenik, K.F. Russell, Intermetallics 13 (3–4) (2005) 387–392.
[12] M.L. Hamilton, D.S. Gelles, R.J. Lobsinger, G.D. Johnson, W.F. Brown, et al., Fabrication Technological Development of the Oxide Dispersion Strengthened Alloy MA957 for Fast Reactor Applications, Pacific Northwest National Laboratory, Richland, WA, 2000, PNL-13168.
[13] T.S. Chou, H.K.D.H. Bhadeshia, Metall. Trans. A 24A (1993) 773–779.
[14] A. Alamo, V. Lambard, X. Averty, M.H. Mathon, J. Nucl. Mater. 329–333 (2004) 333–337.
[15] I.S. Kim, B.Y. Choi, C.Y. Kang, T. Okuda, P.J. Maziasz, et al., ISIJ Int. 43 (2003) 1640–1646.
[16] M.J. Alinger, On the Formation and Stability of Nanometer Scale Precipitates in Ferritic Alloys during Processing and High Temperature Service (Ph.D. Thesis), University of California, Santa Barbara, 2004.
[17] P. Miao, G.R. Odette, T. Yamamoto, M.J. Alinger, D. Hoelzer, et al., J. Nucl. Mater. 367–370 (2007) 208–212.
[18] P. Miao, G.R. Odette, T. Yamamoto, M.J. Alinger, D. Klingensmith, J. Nucl. Mater. 377 (1) (2008) 59–64.
[19] W.J. Yang, G.R. Odette, T. Yamamoto, P. Miao, M.J. Alinger, et al., J. Nucl. Mater. 367–370 (2007) 616–620.
[20] S. Ukai, T. Okuda, M. Fujiwara, T. Kobayashi, S. Mizuta, et al., J. Nucl. Sci. Technol. 39 (2002) 872–879.
[21] S. Ukai, S. Mizuta, M. Fujiwara, T. Okuda, T. Kobayashi, J. Nucl. Sci. Technol. 39 (2002) 778–788.
[22] M.J. Alinger, G.R. Odette, G.E. Lucas, J. Nucl. Mater 307–311 (2002) 484–489.
[23] M.E. Alam, K. Fields, G.R. Odette, D.T. Hoelzer, S.A. Maloy, Tensile Property Characterization of 14YWT Nanostructured Ferritic Alloy NFA1, Fusion Materials Semiannual Progress Report December 31, 2014, DOE/ER-313/57, 2015, pp. 39–48.
[24] S. Pal, M.E. Alam, G.R. Odette, J.J. Lewandowski, D.T. Hoelzer, S.A. Maloy, Characterization of the Microstructures and Textures of NFA-1 for Two Deformation Processing Routes, Fusion Materials Semiannual Progress Report June 30, 2015, DOE/ER-313/58, 2015, pp. 29–41.
[25] L. Toualbi, C. Cayron, P. Olier, J. Malaplate, M. Praud, et al., J. Nucl. Mater. 428 (2012) 47–53.

[26] L. Toualbi, C. Cayron, P. Olier, R. Loge, Y. de Carlan, J. Nucl. Mater. 442 (2013) 410–416.
[27] S. Zherebtsov, A. Mazur, G. Salishchev, W. Lojkowski, Mater. Sci. Eng. A 485 (2008) 39–45.
[28] S. Zherebtsov, G. Salishchev, W. Lojkowski, Mater. Sci. Eng. A 515 (2009) 43–48.
[29] M. Lewandowska, A.T. Krawczynska, M. Kulczyk, K.J. Kurzydłowski, J. Nucl. Mater. 389–388 (2009) 499–502.
[30] J.J. Lewandowksi, B. Berger, J.D. Rigney, S.N. Patankar, Philos. Mag. 78 (3) (1998) 643–656.
[31] R.W. Margevicius, J.J. Lewandowski, I.E. Locci, Scr. Metall. Mater. 29 (1992) 1733–1736.
[32] R.W. Margevicius, J.J. Lewandowski, Scr. Metall. 25 (9) (1991) 2017–2022.
[33] R.W. Margevicius, J.J. Lewandowski, I.E. Locci, R.D. Noebe, Scr. Metall. Mater. 29 (1993) 1309–1312.
[34] B.L. Adams, Ultramicroscopy 67 (1997) 11–17.
[35] V. Kumar, IEEE Trans. Image Process. 22 (7) (2013) 2637–2645.
[36] P.W. Lisowski, K.F. Schoenberg, Nucl. Instr. Methods Phys. Res. A 562 (2) (2006) 910–914.
[37] R. Hielscher, H. Schaeben, J. Appl. Cryst. 41 (2008) 1024–1037.
[38] Z. Oksiuta, P. Hosemann, S.C. Vogel, N. Baluc, J. Nucl. Mater. 451 (2014) 320–327.
[39] D. Orlov, P.P. Bhattacharjee, Y. Takada, M. Umemoto, N. Tsuji, Scr. Mater. 60 (10) (2009) 893–896.
[40] R. Jamaati, M.R. Toroghinejad, M.A. Mohtadi-Bonab, H. Edris, J.A. Szpunar, M. R. Salmani, J. Mater. Eng. Perform. 23 (2014) 4436–4445.
[41] F.J. Humphreys, M. Hatherly, Recrystallization and Related Annealing Phenomena, 2nd ed., Elsevier Science Ltd., Oxford, UK, 2004.
[42] O. Engler, V. Randle, Introduction to Texture Analysis—Macrotexture, Microtexture, and Orientation Mapping', 2nd ed., Taylor & Francis Group, New York, 2010.
[43] J.-Y. Kang, B. Bacroix, H. Regle, K.H. Oh, H.-C. Lee, Acta Mater. 55 (2007) 4935–4946.
[44] M. Holscher, D. Raabe, K. Lucke, Mater. Technol. 62 (1991) 12.
[45] O.A. Bauchau, J.I. Craig, Structural Analysis with Applications to Aerospace Structures, Springer, New York, 2009.
[46] W.B. Hutchinson, Philos. Trans. R. Soc. Lond. A 357 (1999) 1471–1485.
[47] J.L. Raphanel, P. Van.Houtte, Acta Metall. 33 (8) (1985) 1481–1488.
[48] D. Raabe, Mater. Sci. Technol. 9 (1993) 302–314.

Journal of Nuclear Materials 486 (2017) 86–95

Contents lists available at ScienceDirect

Journal of Nuclear Materials

journal homepage: www.elsevier.com/locate/jnucmat

Stability of nanosized oxides in ferrite under extremely high dose self ion irradiations

E. Aydogan [a, *], N. Almirall [b], G.R. Odette [b], S.A. Maloy [a], O. Anderoglu [c], L. Shao [d], J.G. Gigax [d], L. Price [d], D. Chen [d], T. Chen [d], F.A. Garner [d], Y. Wu [b], P. Wells [b], J.J. Lewandowski [e], D.T. Hoelzer [f]

[a] Los Alamos National Laboratory, Los Alamos, NM 87545, USA
[b] University of California, Santa Barbara, Santa Barbara, CA 93106, USA
[c] University of New Mexico, Albuquerque, NM 87131, USA
[d] Texas A&M University, College Station, TX 77843, USA
[e] Case Western Reserve University, Cleveland, OH 44106, USA
[f] Oak Ridge National Laboratory, Oak Ridge, TN 37831, USA

ARTICLE INFO

Article history:
Received 26 August 2016
Received in revised form
8 January 2017
Accepted 9 January 2017
Available online 10 January 2017

ABSTRACT

A nanostructured ferritic alloy (NFA), 14YWT, was produced in the form of thin walled tubing. The stability of the nano-oxides (NOs) was determined under 3.5 MeV Fe^{+2} irradiations up to a dose of ~585 dpa at 450 °C. Transmission electron microscopy (TEM) and atom probe tomography (APT) show that severe ion irradiation results in a ~25% reduction in size between the unirradiated and irradiated case at 270 dpa while no further reduction within the experimental error was seen at higher doses. Conversely, number density increased by ~30% after irradiation. This 'inverse coarsening' can be rationalized by the competition between radiation driven ballistic dissolution and diffusional NO reformation. No significant changes in the composition of the matrix or NOs were observed after irradiation. Modeling the experimental results also indicated a dissolution of the particles.

Published by Elsevier B.V.

1. Introduction

Advanced nuclear systems can provide enhanced energy generation efficiency, safety and reliability, but some reactor designs require improved radiation tolerance of more than 200 displacements per atom (dpa) at high operation temperatures up to 1000 °C [1]. Nanostructured ferritic alloys (NFAs) are attractive materials for Generation IV reactors because of their excellent high temperature strength, thermal stability, creep resistance and radiation tolerance, provided by a high density of Y-Ti-O (<5 nm) nano-oxides (NOs) [2–4]. Atom probe tomography (APT) studies have been interpreted to suggest that NOs are nonstoichiometric phases with low O/(Y + Ti) ratio, while transmission electron microscopy (TEM) and X-ray diffraction (XRD) studies have shown that most NOs are pyrochlore $Y_2Ti_2O_7$ structure having Y/Ti ≈ 1 [5–7].

NOs can pin grain boundaries and dislocations, leading to high strength and superior structural stability [2–4]. Moreover, they may act as recombination centers for both point defects created from neutron damage and trapping sites for helium atoms created by transmutation reactions [2–4]. Overall, NFAs have remarkable radiation tolerance, but the stability of the enabling NOs under extreme irradiation conditions needs to be systematically tested.

The stability of NOs has been studied extensively under both neutron and heavy ion irradiations, but most of these previous studies were limited to moderate damage levels (< 200 dpa). In a brief summary, Yamashita et al. reported that small oxides dissolve under neutron irradiation in 11Cr and 13Cr alloys irradiated in the experimental fast reactor JOYO up to ~20 dpa at 450–561 °C [8]. Yamashita et al. also found that NO density decreases in MA957 after neutron irradiation at 500 °C up to 100 dpa [9]. However, Mathon et al. reported that NOs are stable at 325 °C up to 5.5 dpa in neutron irradiated MA957 [10]. Similarly, Gelles found no significant changes in the NO distribution in MA957 irradiated in the FFTF/MOTA at 420 °C to 200 dpa [11]. Ribis et al. showed that the diameter of the NOs in MA957 are almost the same after neutron irradiation up to 50 and 75 dpa at 412 and 430 °C in the same alloy

* Corresponding author.
E-mail address: aydogan@lanl.gov (E. Aydogan).

http://dx.doi.org/10.1016/j.jnucmat.2017.01.015
0022-3115/Published by Elsevier B.V.

[12–14]. For the same alloy, Bailey et al. reported that, while the diameter and number density of NOs remain almost the same at 550 and 670 °C, the diameter of the NOs decreased just slightly and density increased considerably at 412 °C after ~110 dpa irradiations in FFTF-MOTA [15]. The NOs in 9Cr and 12Cr ODS alloys were also reported to be stable under neutron irradiations at 330–500 °C up to 15 dpa [16]. Similar to the neutron irradiations, NOs were found to be stable after ion irradiation up to 10 dpa at 300 and 500 °C in 12YWT and 19Cr-ODS steels [17,18]. The same behavior was observed in various ferritic ODS alloys for 20 dpa ion irradiations at 200, 500 and 700 °C, as well as for 60 dpa at 650 °C, and for 150 dpa at 670 °C [19–21]. In contrast, Allen et al. concluded that the diameter of the NOs decreases while their density increases at the temperatures 500–700 °C under Ni ion irradiations up to 150 dpa in 9Cr ferritic/martensitic alloys [22]. Parish et al. [23] and Certain et al. [24] reported that at low temperatures (below 300 °C) the NOs dissolve under heavy ion irradiations as a result of ballistic mixing, while at and above 300 °C they are either stable or slightly increased in diameter in 14YWT and 9Cr ODS alloys. On the other hand, He et al. [25] reported that while the size and density of the NOs decrease at 300 °C, NOs are stable at higher temperatures in 14YWT, Ni ion irradiated to 100 dpa.

A significant difference between various studies is that neutrons in test reactors are typically at a damage rate of 10^{-6}-10^{-8} dpa/s, while ion irradiation studies are usually at 10^{-2}-10^{-4} dpa/s. In addition to the dpa rate, temperature, and the size and composition of the NOs are the factors affecting their stability under radiation [26,27]. While there may be a number of heats of MA957, the literature shows that they closely resemble one another as well as the 14YWT alloys with respect to Y-Ti-O NOs with some variability expected for slightly different compositions and processing routes [28]. In this particular case, TEM and APT studies show that the NOs in the 14YWT tubing are very similar to those in MA957.

The references cited above were conducted at different damage rates and with slightly different NO compositions and sizes, thus the issue of NO stability has not been resolved, especially at the temperatures above 300 °C and doses greater than ~200 dpa. In contrast to previous studies, here we examine the irradiation response of a NFA 14YWT under extreme radiation damage levels up to ~585 dpa at 450 °C at a comparable damage rate with the above cited references. Notably, the NFA studied here is in the form of an extruded tube targeting an actual application as fuel cladding.

2. Experimental

The 14YWT heat called FCRD NFA-1, with a nominal composition of 14Cr-3W-0.4Ti-0.21Y-Fe wt.% was developed in an extensive collaboration between Los Alamos National Laboratory, Oak Ridge National Laboratory, University of California, Santa Barbara and Case Western Reserve University. In this work, we examine NFA-1 in the form of tubing that was fabricated by hydrostatic extrusion of a mandrel mounted mother tube cut from an extruded and cross-rolled plate. Further details can be found in Ref. [29].

Samples extracted from the tubes were irradiated at the Texas A&M University Ion Beam Laboratory by 3.5 MeV Fe^{2+} ions to reach peak displacement damage levels of 500, 700, 900 and 1100 dpa at 450 °C. The corresponding ion fluences are 4.9×10^{17}, 6.9×10^{17}, 8.8×10^{17} and 1.1×10^{18} cm^{-2} for 500, 700, 900 and 1100 peak dpa, respectively. The 6 × 6 mm ion irradiated area was achieved by defocusing rather than rastering the beam, since the latter has been shown to suppress void swelling [30–33]. The beam current was controlled at ~200 nA to minimize local heating. The sample temperature was monitored and controlled by a thermocouple mounted on the face of the hot stage that provided feedback to the heater controller. Temperature fluctuations during the irradiation were less than ±5 °C. The peak displacement rate was 1.7×10^{-3} dpa per second.

Fig. 1 shows the calculated damage and Fe implantation profiles for 1100 peak dpa irradiation, obtained from SRIM 2013 code [34]. The SRIM calculations used the Kinchin-Pease model with an Fe displacement energy of 40 eV. The projected range (R_p) of 3.5 MeV Fe^{+2} ions is ~1.2 μm, while the dpa peaks at ~1.0 μm. The injected Fe atoms exceed 10 at.% at depths beyond 700 nm for the 1100 peak dpa irradiation. Therefore, in order to minimize the effects of injected interstitials, the microstructural characterization focused on a sampling depth region from 400 to 600 nm, shown by the shading in Fig. 1. At this depth interval, the concentration of injected atoms, even at 1100 peak dpa, is less than 3 at.%. The average local doses in the sampled region for 500, 700, 900 and 1100 peak dpa were ~270, 375, 480 and 585 dpa, respectively.

The microstructures prior to and after irradiation were characterized by Transmission Electron Microscopy (TEM) and Atom Probe Tomography (APT). Samples were punched in 3 mm disks from the faces of the cladding tubes. Pre-irradiation TEM foils were prepared by mechanical polishing followed by jet electropolishing using a solution of perchloric acid (5%) and methanol at −40 °C with an applied voltage of 20 V. Those foils were thinned down to electron-transparent thickness. Both TEM and APT studies were conducted on those 3-mm electron-transparent TEM foils. On the other hand, the foils for the irradiations were jet electropolished on one side for ~30 s in order to clean the surface, while avoiding forming a deep dimple. After irradiation, standard FIB lift-out techniques, followed by low energy cleaning at 1 kV, were used to prepare the electron transparent TEM samples in an FEI Helios Nanolab 600 dual beam focused ion beam (FIB) instrument. The TEM studies were carried out on a FEI Tecnai F30 TEM operating at 300 kV; a Gatan image filter (GIF) was used for energy filtered TEM (EFTEM) foil thickness measurements. A subset of data was imaged both in EFTEM and bright field (BF) TEM modes and the two techniques agreed with each other within ~10%. However, since BF methods are convenient and have been widely used to image the NOs [35,36 as examples only] (which are a diffracting phase with a lower density than the ferrite matrix), this technique was adopted for characterization of the full test matrix. Notably BF TEM also yields results that compare well with APT data (see below).

APT specimens were prepared from the electropolished foils

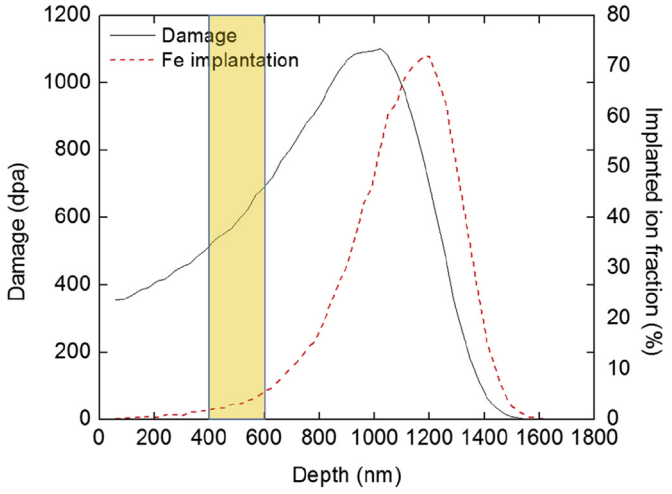

Fig. 1. SRIM-calculated depth profiles of damage and implanted Fe atoms for 1100 peak dpa irradiation in pure Fe. Shaded area shows the sampling depth region from 400 to 600 nm.

using the FIB lift-out technique. Atom probe needles pre-mounted on Si stubs were sharpened via annular milling using decreasing voltage and beam current with a final 2 kV voltage and 28 pA beam current to minimize the surface Ga ion damage. The APT measurements were carried out using a Cameca Local Electrode Atom Probe (LEAP) 3000× HR at 50 K in voltage mode with 200 kHz pulse repetition rate, 0.5–1% evaporation rate, and a 20% pulse fraction.

The 3D APT reconstructions were performed using a commercial Cameca Integrated Visualization and Analysis Software (IVAS) package. The identification of NOs and the corresponding composition analyses were conducted using the maximum separation method for Y, Ti and O ions, as well as their complex ionic forms of TiO and YO [37]. Mass to charge ratio of the time of flight spectrum was used to identify the various ion species associated with the constituent elements in the NFA alloy. NO diameter and composition estimates based on nominal IVAS reconstruction positions have artifacts introduced by trajectory aberrations, and in the case of oxygen due to surface diffusion on the tip. Therefore, an alternative method proposed by Cunningham et al. [38] was used to calculate the NO diameter. The diameter estimates are based on the number of solute atoms in the $Y_2Ti_2O_7$–type phase, corrected for a detector efficiency of 37%. Furthermore, Fe and excess Cr, nominally located in the NO clusters by IVAS, were removed, since they are believed to be an APT artifact associated with the trajectory aberrations. It should be noted that trajectory aberrations are signaled by non-physical high local atom densities that are higher by up to a factor of 3 times that for bcc Fe [39–43]. This procedure may slightly underestimate the Cr content of the features, but this is not expected to have a significant effect on the overall results. The APT reconstructions reveal lower Y/Ti and O/(Ti + Y) ratios in the embedded NOs compared to bulk pyrochlore $Y_2Ti_2O_7$. This may be partially an APT artifact, and partially due to a Ti-rich NO shell [39]. Notably, more recent TEM studies have shown that those NOs are $Y_2Ti_2O_7$ particles with Y/Ti ≈ 1, but with Cr and/or Ti enriched shells [40,43,44].

Statistics were obtained from 200 to 250 NOs for TEM and 200 to 400 NOs for APT studies. The total volume sampled per condition is ~15×10^{-18} m^3 and ~3×10^{-20} m^3 for TEM and APT studies, respectively. The error in the data is calculated as the standard deviation of the mean value.

3. Results

3.1. Microstructure before irradiation

The micrograph in Fig. 2a shows a low magnification BF TEM image of the typical microstructure of 14YWT (heat NFA-1) containing finely distributed NOs together with larger particles. The larger particles are Ti-Si-O-N rich phases with trace amounts of Y [45]. As shown in Fig. 2a, the number density of large particles is quite low compared to that for the NOs. Fig. 2b shows a higher magnification BF TEM image of NOs. The average diameter and density of the NOs in the unirradiated 14YWT were estimated to be ~2.8 ± 0.7 nm and ~4.3 ± 0.7 × 10^{23} m^{-3}, respectively.

Due to their small diameter, it is extremely difficult to establish the detailed structure, composition and interface character of the small NOs. A recent paper by Wu et al. [28] reported the presence of $Y_2Ti_2O_7$, consistent with much of the literature that generally involve larger NOs. Notably, however, Fast Fourier Transform (FFT) power spectra for large matrix regions containing many small NOs produced extra diffraction spots consistent with defected pyrochlore $Y_2Ti_2O_7$. It has been shown that one large and one smaller NOs have a clear cube-on-edge orientation relationship. Detailed through focus exit wave analysis found a pyrochlore structure in the larger NO, with a 5 × 7 near coincidence site lattice interface. It has been reported by many authors that there is a relationship between NO diameter and their corresponding coherency with the matrix. Small NOs are often reported to be coherent, as expected, while transitioning to semicoherent, or even incoherent interfaces as the diameter increases. It was also found by Wu et al. [28] that coherency/semicoherency strains increased with decreasing diameter.

Detailed NO diameters, number densities and compositions were obtained by 3D APT studies. 3 to 10 tips were investigated for each condition, depending on the variability of the microstructure. For instance, the distribution of the NOs in the unirradiated condition was relatively less homogenous for the tips in this study, thus requiring 10 tips to obtain good statistics. On the other hand, the samples irradiated to various dpa do not seem to show as large microstructural variations, therefore, only 3–4 tips were investigated. Each condition has an average count of ~4 million atoms. Fig. 3 is a representative APT reconstruction for the unirradiated 14YWT showing the solute distributions and NO clusters. Note the

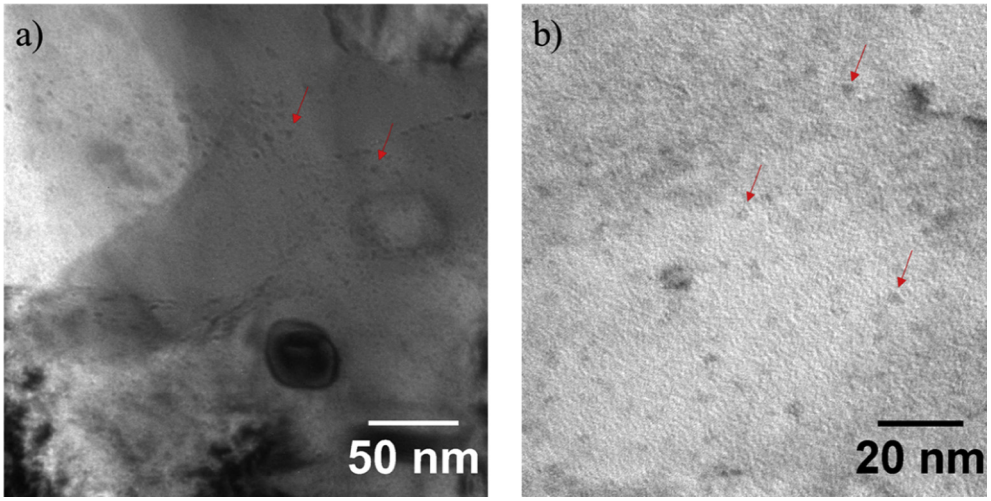

Fig. 2. Distribution of particles before irradiation. (a) Low magnification BF TEM image showing both larger particles and NOs (b) high magnification image showing the NO distribution. Arrows point the NOs.

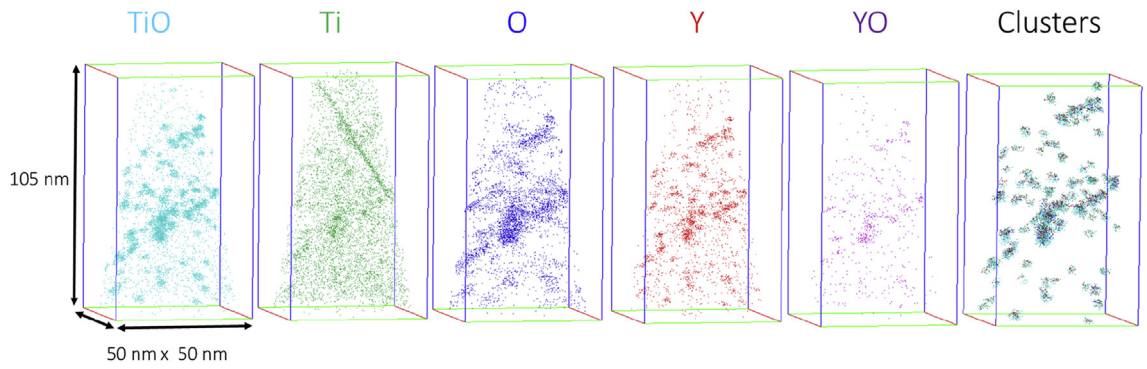

Fig. 3. APT 3D reconstruction of unirradiated 14YWT samples showing the distribution of various elements, ions and NO clusters.

Table 1
Compositions (at.%) of the matrix and NOs in unirradiated condition as determined by APT analyses.

Element (at.%)	Matrix composition	NO composition
Fe	83.92 ± 0.15	≈0 (nominal)
O	0.13 ± 0.01	29.86 ± 9.43
Cr	14.72 ± 0.13	18.00 ± 8.82
Ti	0.12 ± 0.01	38.13 ± 6.97
Y	0.02	11.74 ± 4.74
Si	0.06	0.40 ± 0.59
W	0.92 ± 0.01	0.82 ± 1.57
Mn	0.02	0.11 ± 0.29
C	0.04 ± 0.01	0.43 ± 0.69
Al	0.01	0.45 ± 0.63
Y/Ti/O	–	13/45/42

oxygen distribution associated with the NOs is relatively diffuse, which is likely an APT artifact [40]. The APT reconstructions show that the NO distribution is somewhat inhomogeneous in the grains. The NOs and alloying elements often lie on and segregate to grain boundaries. The APT average diameter and number density of the NOs are ~2.1 ± 0.5 nm and ~6.2 ± 1.5 × 10^{23} m^{-3}, respectively.

The APT compositions of the matrix and NOs are summarized in Table 1. Even after composition correction, the NOs still contain a considerable amount of Cr. It is not possible to reliably determine if the Cr is located in the NO core or segregated in the matrix at its interface, as widely reported [44,46]. Although TEM and XRD characterizations in the literature show that the small NOs are mostly $Y_2Ti_2O_7$ [5–7], APT characterization in this study measures Y/Ti/O ratio as 13/45/42. A composition deficiency of Y and O has been reported by many authors and partially attributed to the trajectory aberrations and O surface diffusion, as noted previously [38]. It should also be noted that the composition of the matrix is quite consistent for different tips while the compositions of NOs show large variations from cluster to cluster.

3.2. Microstructures after irradiation

BF TEM micrographs of irradiated samples at various dpa levels are shown in Fig. 4. While irradiations up to 480 dpa result in similar oxide diameters and distributions, as seen in Figs. 4a–c, visual inspection qualitatively suggests that 585 dpa irradiation refines the NOs with smaller diameters and larger number densities as suggested in Fig. 4d. The average diameter and number densities of the NOs obtained by TEM are summarized in Supplementary Table S1 in Appendix A. The TEM measurements show that diameter of the NOs decreases, while their number density increases, with increasing dose at 450 °C. Specifically, the NO diameter decreases from an unirradiated average of ~2.8 ± 0.7 nm to ~2.1 ± 0.6 nm after the irradiations at 270, 375 and 480 dpa irradiations, and further decreases to ~1.7 ± 0.4 nm after the 585 dpa irradiation. The corresponding NO number density increases from ~4.3 ± 0.7 × 10^{23} m^{-3} in the unirradiated condition to ~8.3 ± 1.6 × 10^{23} m^{-3} at 585 dpa. The NO volume fraction also increases from the unirradiated value of 0.53% to 0.69%. Supplementary Table S1 also summarizes the corresponding APT results, which are further discussed below.

Figs. 5a–c show the representative APT reconstructions of 270, 480 and 585 dpa irradiated conditions. The particle distribution after the irradiations appears to be somewhat more homogenous compared to the unirradiated condition. The NO diameter and density tabulated in the Supplementary Table S1 are broadly similar to the TEM results. The APT data also indicate that the diameter of the NOs decreases slightly after irradiation, while their number density increases. While there are moderate differences at lower dpa, the TEM and APT data are remarkably consistent in the 585 dpa condition. Similar to the previous findings [22,47–49], even if initially slightly refined, NOs are more stable above a certain damage level.

Fig. 6 compares the NO diameter distributions obtained by APT and BF TEM analyses. The differences between TEM and APT results are somewhat more apparent than reflected in the average diameter and number density values. However, in both cases before irradiation, the NOs have a broader diameter distribution up to ~5 nm; in contrast, the diameter distribution of NOs after irradiation is narrower and limited to diameters below 4 nm (TEM) and 3 nm (APT) at the highest two dpa. There is also a corresponding increase in the NO diameters below 1.5 nm. The most significant change in the diameter distribution occurs at the lowest dose (270 dpa), especially for the TEM data, but is reasonably stable thereafter, especially for the APT data. Clearly, TEM gives slightly larger diameters compared to APT, likely due to a lower resolution limit. Thus it is notable that TEM observes the same diameter and similar number density in the case of the 585 dpa condition. It should be noted that 375 dpa APT data was not acquired due to limited time and instrumental availability. However, the overall APT trends in NO size and number density are established by higher and lower dpa data and that is reasonably consistent with the TEM data trends.

The standard deviations in the TEM data are larger than that of the APT results, and in most cases they are more than the absolute differences at various dpa. The APT data are probably more reliable, but the sampling volume is very small. On the other hand, TEM gives 2-dimensional data while APT provides 3-dimensional data. However, it is still possible to statistically test the hypothesis by plotting the variations in the mean data. Fig. 7 plots the trends in NO diameter and number density. Fig. 7a shows the diameter as a

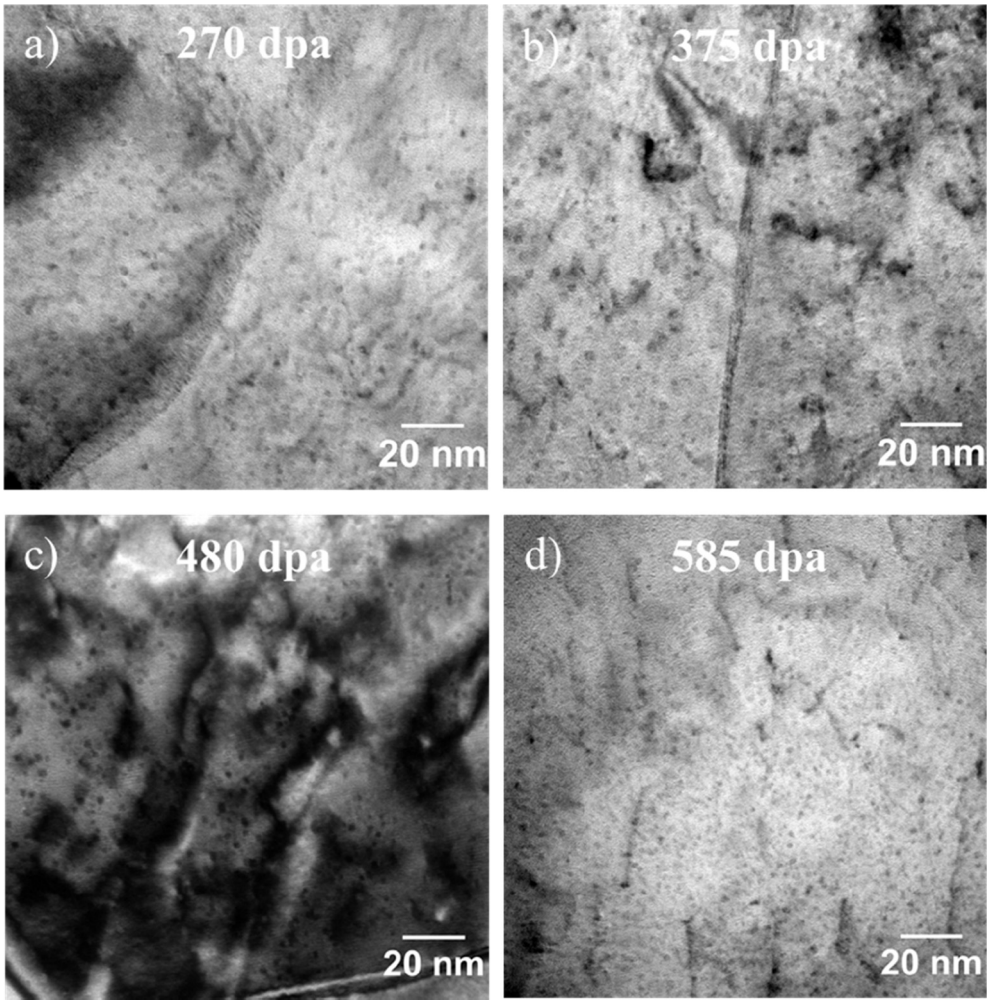

Fig. 4. BF TEM images of samples collected from the depth region of 400 nm–600 nm, after irradiation to (a) 270 dpa (b) 375 dpa (c) 480 dpa and (d) 585 dpa at 450 °C.

function of dpa and Fig. 7b shows the corresponding number density plot for both APT and TEM data. If the fit includes data from the unirradiated condition, the slopes are negative for size and positive for number density, for both the TEM and APT data. The magnitudes of the slopes are larger for the TEM-based data points.

The changes in the size (diameter) distribution of NOs are also subtle but may be even more significant. Fig. 8a plots the fraction of NOs larger than 3 nm for the TEM data and 2.5 nm for the APT data as a function of dpa. Fig. 8b plots the corresponding fraction of NOs less than 2 and 1.5 nm. While somewhat *ad hoc*, these 'larger than and smaller than' fractions are concrete metrics of the effects of ion irradiation on the tails in the distribution of NO sizes. Both APT and TEM indicate that there is a clear and statistically significant trend towards refinement of the NO size distribution.

Thus in spite of the data scatter for the particular conditions, and the expected variability in each sample, region-to-region as well as sample-to-sample, the results lend significant statistical support to the hypothesis that self-ion irradiations at 450 °C with dose rates significantly higher than neutron irradiation cause some dissolution of the NOs as indicated by a change in NO size and number density and a sharpening of the size distribution. It should be noted that on average the largest change in size and number density occurs between 0 and 270 dpa and the changes after this condition seem to be quite small. This may support the conclusion that after an initial transient, the NOs are approaching a quasi-steady state between NO dissolution by ion mixing and self-healing.

The compositions of the matrix and NOs before and after irradiation are summarized in Table 2. Following irradiation, the Cr content of both the matrix and NOs decreases slightly. This is shown in Fig. 9, where Figs. 9a and b show the composition changes in NOs and matrix, respectively. Fig. 9a shows that Cr decreases, O increases, and Ti and Y vary but with no systematic trend. Fig. 9b shows that the Cr decrease is balanced by an Fe increase, as expected. The matrix Fe fraction increases due to the injected interstitials which can reach up to ~3 at.% at the depth of 400–600 nm for the 585 dpa irradiation condition. There may also be some segregation of Cr at grain boundaries. Table 2 shows that the nominal NO Y/Ti/O ratio of the sample is unaffected by irradiation, with average of 13/45/42 for unirradiated condition and 13/44/43 following irradiations. It should be noted that the low Y/Ti ratio is likely, in large part, due to an APT artifact. Thus the APT results are consistent with the TEM analysis showing that the crystal structure of small NO cores below 5 nm are a cubic pyrochlore $Y_2Ti_2O_7$ complex with some possible Ti (and Cr) rich surrounding shell [40,43,44].

4. Discussion: stability of NOs under irradiation

The stability of NOs under irradiation can be predicted from Nelson-Hudson-Mazey (NHM) precipitation model, which

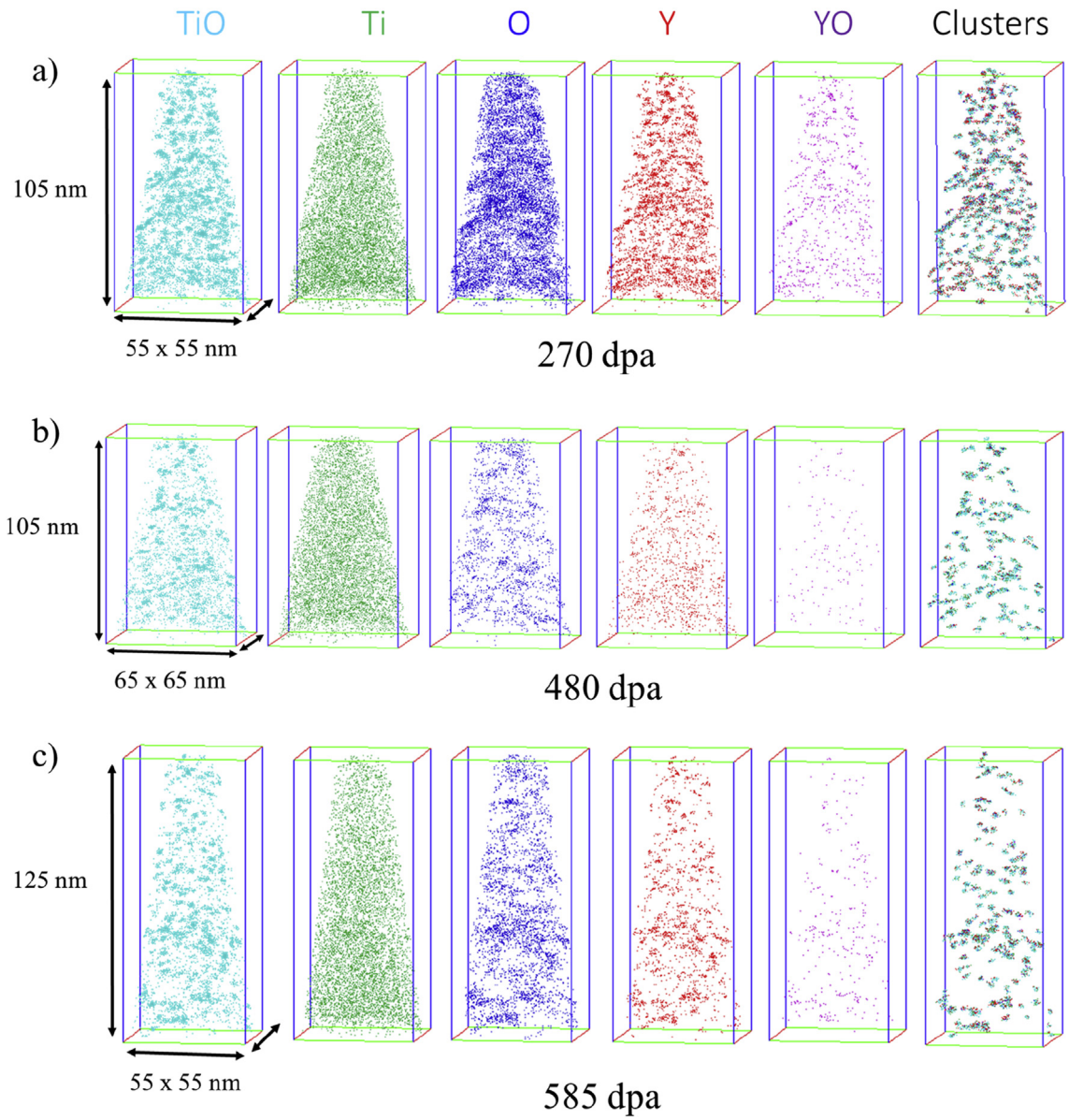

Fig. 5. APT 3D reconstructions showing the distribution of various elements, ions and NO clusters in 14YWT samples irradiated to (a) 270 dpa (b) 480 dpa and (c) 585 dpa at 450 °C.

considers both shrinkage and growth, due to ballistic collision induced dissolution and thermal diffusion induced recovery of precipitates [50]. In agreement with the observations, the model predicts that large NOs shrink and small ones grow under irradiation, reaching an equilibrium diameter which depends on various irradiation parameters. The simple NHM model assumes that the solute flow as a result of ballistic effects is only from particle to the matrix and it ignores the solute fluxes from matrix as a result of dissolution of other particles. This assumption seems to be reasonable as the average mean free distance between the NOs is ~25 nm. Moreover, it ignores the local equilibrium solute concentrations at the solute/matrix interfaces and it does not consider the effects of interface coherency. Chen et al. [47,51] suggest that small NOs are dominated by coherent and semi-coherent interfaces, while the large oxides are incoherent. Since the NOs in the present study are relatively small (less than 5 nm as shown in Fig. 6), the complexity in interface energy changes due to transition from incoherency to coherency is ignored. If the unirradiated interface is coherent, irradiation produces a roughened diffuse interface leading to an increase in the corresponding surface energy along with the solubility of the various NO constituents, while their stability would decrease. However, this can be approximately accounted for in the simple model parameterization. Hence the decay and growth competition can be described by Refs. [52,53]:

$$\frac{dr}{dt} = -G\Psi + \frac{3D'c}{4\pi rp} \tag{1}$$

Here r is the NO radius, G is defect production rate, Ψ is the ballistic dissolution parameter, D' is irradiation enhanced diffusion coefficient, c is the atomic concentration of solute in solution, and p is the solute atom fraction in the NO. The first term on the right side of the equation describes the dissolution rates and the second term describes the reformation kinetics. Both dissolution and growth are largely limited by Y and Ti dissolution and diffusion. Substitutional atoms diffuse by a vacancy diffusion mechanism, hence Y and Ti diffusivity scales with the vacancy supersaturation. In contrast, O

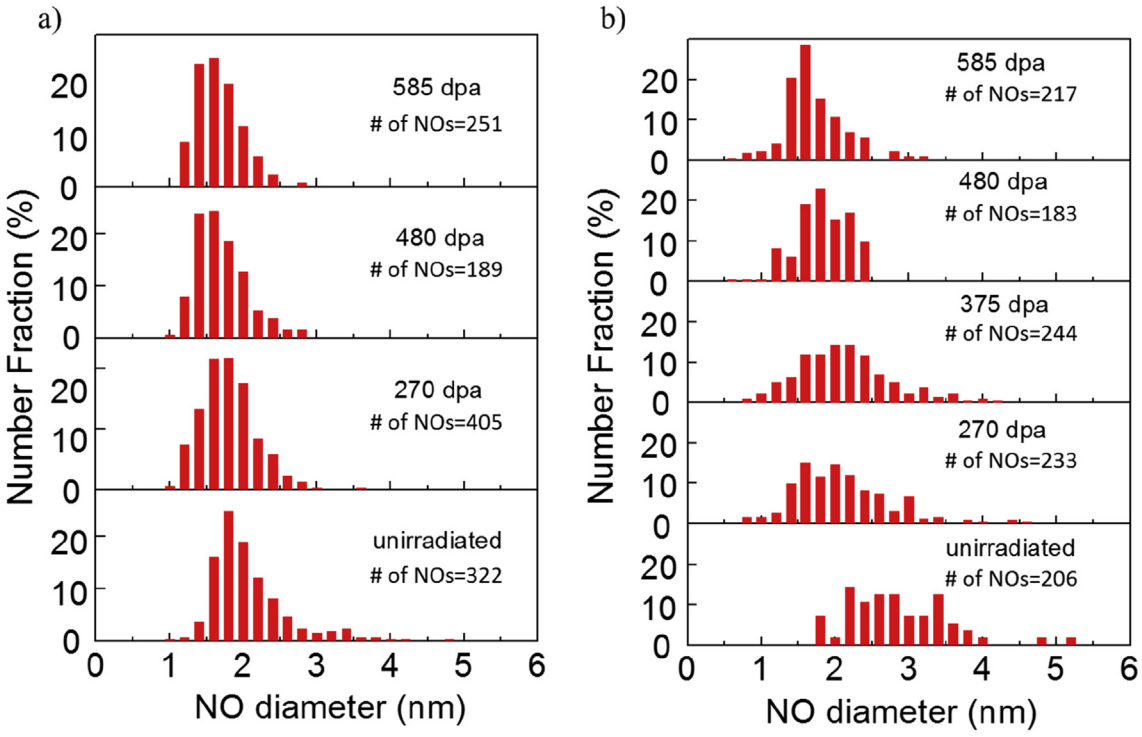

Fig. 6. NO diameter distribution in unirradiated and various dose irradiated samples obtained by (a) APT and (b) TEM analyses.

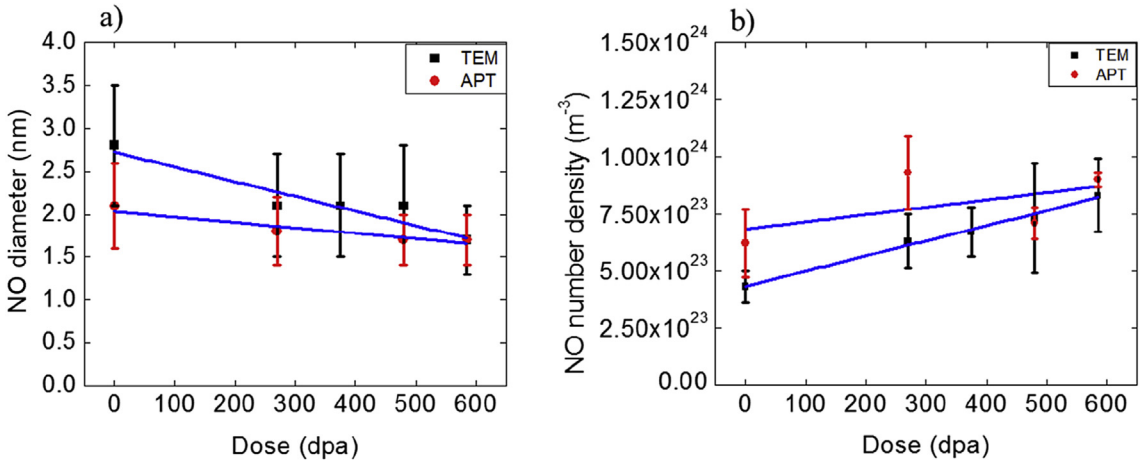

Fig. 7. Linear regression fits to (a and b) NO diameter and number density vs. dpa for both the TEM and APT data.

atoms are fast interstitial diffusers, and can quickly migrate to accommodate any precipitate changes. D' can be approximated by the diffusivity of Y atoms, described by Ref. [36];

$$D' = \frac{C_v'}{C_v^{eq}} D^{th} \tag{2}$$

where C_v' is non-equilibrium concentration of vacancies under irradiation; C_v^{eq} is equilibrium concentration of vacancies; D^{th} is the Y (and Ti) thermal diffusivity under equilibrium condition.

Determination of C_v' requires solving the defect balance equations, which consider defect generation, matrix interstitial-vacancy recombination and defect annihilation or recombination at sinks and trapping sites. At the temperatures where defect diffusion is possible and in the presence of a high density of NOs, the numerical solution leads to a quasi-steady state of vacancy concentration $C_v' = G/(k_{vs}C_s)$, where G is defect creation rate, k_{vs} is vacancy annihilation rate per NO, and C_s is the NO sink concentration. Further details on the numerical calculation to obtain C_v' can be found in Ref. [53]. Note, here we assume the main vacancy sink sites are precipitates that act as fully efficient trapping sites for recombination (since TEM does not observe significant voids and dislocation sink strengths are relatively low). C_s is the NO density. The vacancy-NO reaction rate can be calculated by $k_{vs} = 4\pi r D_V$, where r is NO radius and D_V is vacancy diffusivity. Based on these approximations, equation (2) can be rewritten as;

$$D' = K\left(4\pi r D_V N C_V^{eq}\right)^{-1} D^{th} \tag{3}$$

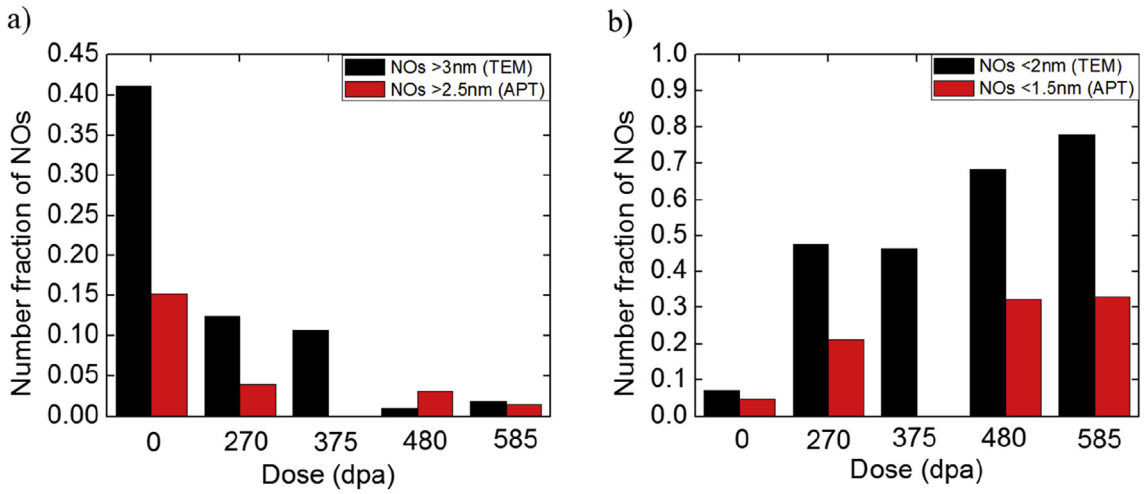

Fig. 8. Changes in the fractions of sizes under irradiation for NOs (a) larger than 3 nm for TEM measurements and 2.5 nm for APT measurements; and, (b) smaller than 2 nm for TEM measurements and 1.5 nm for APT measurements.

Table 2
Compositions (at.%) of the matrix and NOs in unirradiated and irradiated 14YWT samples at 450 °C up to 270, 480 and 585 local dpa doses at the depth of 400–600 nm.

Element (at%)	0 dpa		270 dpa		480 dpa		585 dpa	
	Matrix	NO	Matrix	NO	Matrix	NO	Matrix	NO
Fe	83.92 ± 0.15	0 (nominal)	84.52 ± 1.91	0 (nominal)	86.67 ± 4.14	0 (nominal)	88.32 ± 2.07	0 (nominal)
O	0.13 ± 0.01	29.86 ± 9.43	0.19 ± 0.08	35.63 ± 4.84	0.10 ± 0.03	36.76 ± 5.36	0.14 ± 0.05	35.04 ± 4.87
Cr	14.72 ± 0.13	18.00 ± 8.82	13.98 ± 1.96	7.23 ± 8.20	11.93 ± 4.36	11.52 ± 9.46	10.31 ± 2.24	12.11 ± 9.94
Ti	0.12 ± 0.01	38.13 ± 6.97	0.20 ± 0.02	37.93 ± 6.40	0.15 ± 0.05	40.69 ± 7.08	0.19 ± 0.06	39.30 ± 6.30
Y	0.02	11.74 ± 4.74	0.03 ± 0.01	16.52 ± 9.02	0.01	8.84 ± 6.04	0.02	11.54 ± 5.63
Si	0.06	0.40 ± 0.59	0.05 ± 0.01	0.48 ± 0.78	0.02 ± 0.02	0.47 ± 1.04	0.03 ± 0.01	0.59 ± 1.08
W	0.92 ± 0.01	0.82 ± 1.57	0.91 ± 0.06	0.15 ± 0.88	1.03 ± 0.20	0.16 ± 0.76	0.88 ± 0.08	0.09 ± 0.35
Mn	0.02	0.11 ± 0.29	0.02	0.08 ± 0.33	0.01 ± 0.01	0.13 ± 0.47	0.01	0.08 ± 0.33
C	0.04 ± 0.01	0.43 ± 0.69	0.05	0.37 ± 0.67	0.03 ± 0.01	0.86 ± 2.08	0.07 ± 0.03	1.13 ± 1.96
Al	0.01	0.45 ± 0.63	0.02 ± 0.01	0.43 ± 0.71	0.03 ± 0.02	0.83 ± 1.22	0.02	0.38 ± 0.91
Y/Ti/O	–	13/45/42	–	15/44/42	–	11/44/45	–	13/45/42

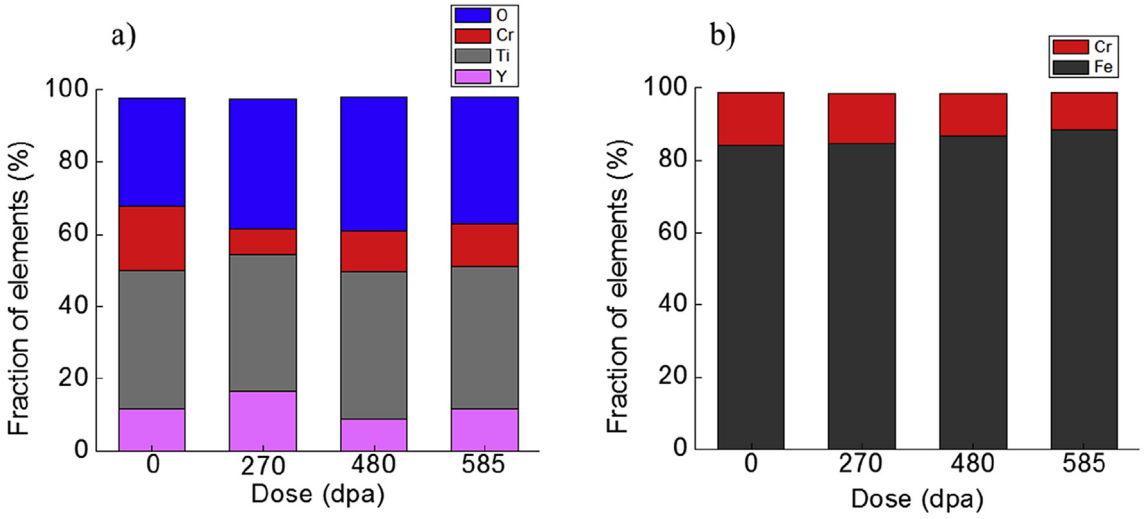

Fig. 9. Graphical representation of composition changes in (a) NOs (b) matrix.

$$D_v = \alpha a^2 \upsilon \exp\left(-\frac{E_v^m}{k_B T}\right) \quad (4)$$

From APT characterization, we can obtain an average NO radius, r, and an average number density, N. The vacancy (and interstitial) generation rate of 9.7×10^{-4} dpa/s was obtained from SRIM calculations. However, Stoller found that the effective dpa rate is about 1/3 of defect generation rate due to the in-cascade recombination in iron [54]. The vacancy diffusivity D_V is calculated by using pre-

exponential entropy and correlation factor, $\alpha = 1$, a jump attempt frequency, $\nu = 10^{13}\ s^{-1}$, and vacancy migration energy, $E_v^m = 0.7$ eV [53,55].

The equilibrium vacancy concentration C_V^{eq} is taken as $C_v^{eq} = N\exp\left(\frac{E_v^f}{k_B T}\right)$ where N is the atomic density and E_v^f is the vacancy formation energy, 2.2 eV in bcc Fe [55]. The thermal diffusivity of Y is taken as $D^{th} = 10^{-5} \times \exp(-3.25eV/k_BT)\ m^2/s$ [56]. Note these parameters are not individually rigorous. For example, the slow diffusion rate of Y assumed here has been contradicted by both first principles calculations, limited measurements and atomistic models fit to NO precipitation and coarsening data [57]. However, use of the cited parameter set is within the spirit of the simple model presented here.

Under a quasi-steady state of NO growth, the growth and dissolution reaches a balance with $dr/dt = 0$ in equation (1). The present experimental study shows that after the radiation damage of 270 dpa and beyond, the mean diameter of NOs is saturated to about 1.7 nm and the average dispersoid density is saturated to about $8.5 \times 10^{23} m^{-3}$. Substituting these two values into the above stated equations for T = 450 °C, we calculate the dissolution parameter Ψ to be 1.5×10^{-12} m.

Once the dissolution parameter is known, the equation of steady state equilibrium (dr/dt = 0) can be found as $r^2N = 1.69 \times 10^6 \exp\left(-\frac{4062}{T}\right)$. Fig. 10 plots Nr^2 vs. T, with the solid line representing the equilibrium condition when growth and dissolution are in balance. The curve is obtained by using the Ψ value determined as described by the previous discussion. For the region above the curve, dissolution dominates and the NOs will shrink until r and N evolve to the steady state condition specified by the line. Below the curve, NOs grow under ion irradiation. In Fig. 10, Nr^2 value of the as-received sample is shown and the arrow shows the trajectory of NO changes under given irradiation conditions.

Fig. 10 is in agreement with previous experimental studies showing that NOs shrink under ion irradiation and, as a function of ion irradiation temperature, the final equilibrium diameters will increase with increasing temperatures, as shown by Chen et al. recently on 12Cr ODS alloys [47,51]. The irradiation parameters Ψ and K depend on specific experimental conditions. Hence the equilibrium curve will shift under different irradiation conditions. On the other hand, if parameter difference and their conversions under different conditions, such as accelerator ion irradiation vs. reactor neutron irradiation, are known, in principle the prediction on stability of NOs is possible from accelerated testing at higher dpa rates. In addition to the fact that the current model does not consider the role of interface coherency, the effects from void swelling are ignored since even for the highest dpa, we barely see small bubble formation [45]. For other ODS systems which have much more void swelling, such as MA956, the discussion on sink strength must consider vacancy-void interactions. Therefore, the current model presents a simplified approach to predict NO stability.

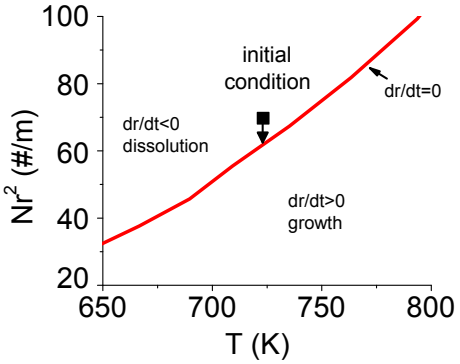

Fig. 10. Nr^2 vs. T plot showing the behavior of the NOs in the present study.

Slight increase in the density of the NOs after irradiation might indicate that the dissolved atoms form new NOs instead of growing the previously existing ones. Similar 'inverse coarsening' behavior was first observed by Frost and Russell [58] due to the radiation induced ejection of solute atoms from the particles into the matrix, and diffusion of this solute back to and away from the particle. Li et al. [59] reported that in thermally-aged CF8 steels irradiated with 1 MeV Kr ions, the size of the G-phase precipitates decreased while their density increased. Moreover, Tan et al. [60] found that the ejected atoms from original TaC nanoscale precipitates by displacement cascade led to a reduction in the size of the original carbides and provided matrix solutes to nucleate new precipitates, thereby increasing their corresponding density. However, uncertainties in both the data itself, and simplicity of the model and its approximate parameterization, do not support rigorous quantitative conclusions. The most important result by far, is the remarkable stability of the NOs even at very high dpa levels and at high dpa rates.

5. Conclusions

14YWT NFA-1 in tube form was irradiated to very high doses up to ~585 dpa at 450 °C and the stability of NOs have been investigated via TEM and APT techniques. The results from these analyses suggest that self-ion irradiations result in ~25% decrease in the NO diameter coupled with ~30% increase in their number density. On average the largest decrease occurs over the initial dose increment from 0 to 270 dpa. This behavior has been rationalized by the 'inverse coarsening' phenomena due to the disruption of balance between irradiation induced ejection of solute atoms out of the NOs and thermal diffusion of this solute back to the particle, consistent with the simple steady-state model prediction. The calculations predicting an increase in the NO density and the decrease in their diameter indicate some degree of dissolution and re-precipitation. However, NOs were found to be extremely stable even under very high dpa levels at 450 °C.

Acknowledgments

This research was partially supported by DOE-NE Fuel Cycle Research and Development Program under the Contract number DE-AC52-06NA25396. Research at TAMU is supported by US Department of Energy (DOE), NEUP program, through grant no. DE-NE0008297. Research at UCSB was sponsored by the US DOE, Office of Fusion Energy Sciences and the Office of Nuclear Energy. The FIB and APT were performed in the UCSB MRL Shared Experimental Facilities at UCSB supported by the NSF MRSEC Program. The authors would like to give special thanks to UCSB's Dr. N. Cunningham for his guidance and help for the APT studies and Dr. X. Wang for her helps on irradiations at Ions and Materials Laboratory, TAMU.

Appendix A. Supplementary data

Supplementary data related to this article can be found at http://dx.doi.org/10.1016/j.jnucmat.2017.01.015.

References

[1] T.R. Allen, J.T. Busby, R.L. Klueh, S.A. Maloy, M.B. Toloczko, JOM 60 (2008)

15–23.
[2] G.R. Odette, M.J. Alinger, B.D. Wirth, Annu. Rev. Mater. Res. 38 (2008) 471–503.
[3] G.R. Odette, D.T. Hoelzer, JOM 62 (2010) 84–92.
[4] G.R. Odette, JOM 66 (2014) 2427–2441.
[5] Y. Wu, E.M. Haney, N.J. Cunningham, G.R. Odette, Acta Mater. 60 (2012) 3456–3468.
[6] A.J. London, B.K. Panigrahi, C.C. Tang, C. Murray, C.R.M. Grovenor, Scr. Mater. 110 (2016) 24–27.
[7] M. Ohnuma, J. Suzuki, S. Ohtsuka, S.W. Kim, T. Kaito, M. Inoue, H. Kitazawa, Acta Mater. 57 (2009) 5571–5581.
[8] S. Yamashita, K. Oka, S. Ohnuki, N. Akasaka, S. Ukai, J. Nucl. Mater. 307–311 (2002) 283–288. Part 1.
[9] S. Yamashita, N. Akasaka, S. Ukai, S. Ohnuki, J. Nucl. Mater. 367–370 (2007) 202–207. Part A.
[10] M.H. Mathon, Y. De Carlan, X. Averty, A. Alamo, C.H. De Novion, J. ASTM Int. 2 (2005) 213–227.
[11] D.S. Gelles, Fusion Reactor Materials Semiannual Progress Report for the Period Ending March 31 DOE/ER-0313/16, 1994, p. 146.
[12] J. Ribis, J. Nucl. Mater. 434 (2013) 178–188.
[13] J. Ribis, S. Lozano-Perez, Mater. Lett. 74 (2012) 143–146.
[14] J. Ribis, S. Lozano-Perez, J. Nucl. Mater. 444 (2014) 314–322.
[15] N.A. Bailey, E. Stergar, M. Toloczko, P. Hosemann, J. Nucl. Mater. 459 (2015) 225–234.
[16] N. Akasaka, S. Yamashita, T. Yoshitake, S. Ukai, A. Kimura, J. Nucl. Mater. 329–333 (2004) 1053–1056. Part B.
[17] P. Pareige, M.K. Miller, R.E. Stoller, D.T. Hoelzer, E. Cadel, B. Radiguet, J. Nucl. Mater. 360 (2007) 136–142.
[18] K. Yutani, R. Kasada, H. Kishimoto, A. Kimura, J. ASTM Int. 4 (2007).
[19] A. Kimura, H.-S. Cho, N. Toda, R. Kasada, K. Yutani, H. Kishimoto, N. Iwata, S. Ukai, M. Fujiwara, J. Nucl. Sci. Technol. 44 (2007) 323–328.
[20] H. Kishimoto, R. Kasada, O. Hashitomi, A. Kimura, J. Nucl. Mater. 386–388 (2009) 533–536.
[21] H. Kishimoto, K. Yutani, R. Kasada, O. Hashitomi, A. Kimura, J. Nucl. Mater. 367–370 (2007) 179–184. Part A.
[22] T.R. Allen, J. Gan, J.I. Cole, M.K. Miller, J.T. Busby, S. Shutthanandan, S. Thevuthasan, J. Nucl. Mater. 375 (2008) 26–37.
[23] C.M. Parish, R.M. White, J.M. LeBeau, M.K. Miller, J. Nucl. Mater. 445 (2014) 251–260.
[24] A. Certain, S. Kuchibhatla, V. Shutthanandan, D.T. Hoelzer, T.R. Allen, J. Nucl. Mater. 434 (2013) 311–321.
[25] J. He, F. Wan, K. Sridharan, T.R. Allen, A. Certain, V. Shutthanandan, Y.Q. Wu, J. Nucl. Mater. 455 (2014) 41–45.
[26] W. Xu, L. Li, J.A. Valdez, M. Saber, Y. Zhu, C.C. Koch, R.O. Scattergood, J. Nucl. Mater. 469 (2016) 72–81.
[27] S. Yamashita, N. Akasaka, S. Ohnuki, J. Nucl. Mater. 329–333 (2004) 377–381. Part A.
[28] Y. Wu, J. Ciston, S. Kräemer, N. Bailey, G.R. Odette, P. Hosemann, Acta Mater. 111 (2016) 108–115.
[29] E. Aydogan, S. Pal, O. Anderoglu, S.A. Maloy, S.C. Vogel, G.R. Odette, J.J. Lewandowski, D.T. Hoelzer, I.E. Anderson, J.R. Rieken, Mater. Sci. Eng. A 661 (2016) 222–232.
[30] J.A. Sprague, F.A. Smidt Jr., Naval Research Laboratory Semi-annual Progress Report, NRL Memorandum Report, vol. 2629, November 1972-April 1973, p. 27.
[31] ASTM E521-83.Standard Practice for Neutron Radiation Damage Simulation by Charged-particle Irradiation. West Conshohocken, ASTM International.
[32] E. Getto, Z. Jiao, A.M. Monterrosa, K. Sun, G.S. Was, J. Nucl. Mater. 465 (2015) 116–126.
[33] J.G. Gigax, E. Aydogan, T. Chen, D. Chen, L. Shao, Y. Wu, W.Y. Lo, Y. Yang, F.A. Garner, J. Nucl. Mater. 465 (2015) 343–348.
[34] J.F. Ziegler, J.P. Biersack, SRIM2006: the Stopping and Range of Ions in Matter: Version, 2006 available at: http://www.srim.org.
[35] J. Ribis, Y. De Carlan, Acta Mater. 60 (2012) 238–252.
[36] M.L. Lescoat, J. Ribis, Y. Chen, E.A. Marquis, E. Bordas, P. Trocellier, Y. Serruys, A. Gentils, O. Kaïtasov, Y. De Carlan, A. Legris, Acta Mater. 78 (2014) 328–340.
[37] D. Vaumousse, A. Cerezo, P.J. Warren, Ultramicroscopy 95 (2003) 215–221.
[38] N. Cunningham, Y. Wu, D. Klingensmith, G.R. Odette, Mater. Sci. Eng. A 613 (2014) 296–305.
[39] N.J. Cunningham, Study of Structure, Composition, and Stability of Y–Ti–O nm-scale Features in Nano-structured Ferritic Alloys, Ph.D. Thesis, University of California, Santa Barbara, 2012.
[40] C.A. Williams, E.A. Marquis, A. Cerezo, G.D.W. Smith, J. Nucl. Mater. 400 (2010) 37–45.
[41] N.C.P. Wells, G.R. Odette, Recent Progress on Understanding and Quantifying Atom Probe Tomography Artifacts for High Evaporation Rate nm-scale Phases in Fe Based Alloys, Fusion Materials Semiannual Progress Report for the Period Ending December31, 2011. DOE-ER-0313/51;2012.
[42] C. Oberdorfer, G. Schmitz, Microsc. Microanal. 17 (2011) 15–25.
[43] E.A. Marquis, Appl. Phys. Lett. 93 (2008).
[44] A.J. London, S. Lozano-Perez, M.P. Moody, S. Amirthapandian, B.K. Panigrahi, C.S. Sundar, C.R.M. Grovenor, Ultramicroscopy 159 (2015) 360–367. Part 2.
[45] E. Aydogan, S.A. Maloy, O. Anderoglu, C. Sun, J.G. Gigax, L. Shao, F.A. Garner, I.E. Anderson and J.J. Lewandowski, 'Effect of Tube Processing Methods on Microstructure, Mechanical Properties and Irradiation Response of 14YWT Nanostructured Ferritic Alloys' in Preparation.
[46] V. Badjeck, M.G. Walls, L. Chaffron, J. Malaplate, K. March, J. Nucl. Mater. 456 (2015) 292–301.
[47] T. Chen, E. Aydogan, J.G. Gigax, D. Chen, J. Wang, X. Wang, S. Ukai, F.A. Garner, L. Shao, J. Nucl. Mater. 467 (2015) 42–49.
[48] K. Mo, Z. Zhou, Y. Miao, D. Yun, H.M. Tung, G. Zhang, W. Chen, J. Almer, J.F. Stubbins, J. Nucl. Mater. 455 (2014) 376–381.
[49] Y. Miao, K. Mo, Z. Zhou, X. Liu, K.C. Lan, G. Zhang, M.K. Miller, K.A. Powers, J. Almer, J.F. Stubbins, Mater. Sci. Eng. A 625 (2015) 146–152.
[50] R.S. Nelson, J.A. Hudson, D.J. Mazey, J. Nucl. Mater. 44 (1972) 318–330.
[51] T. Chen, J.G. Gigax, L. Price, D. Chen, S. Ukai, E. Aydogan, S.A. Maloy, F.A. Garner, L. Shao, Acta Mater. 116 (2016) 29–42.
[52] F.S. Ham, J. Phys. Chem. Solids 6 (1958) 335–351.
[53] G.S. Was, Fundamentals of Radiation Materials Science : Metals and Alloys, Springer, Berlin, 2007.
[54] R.E. Stoller, J. Nucl. Mater. 233–237 (1996) 999–1003.
[55] F. Soisson, C.C. Fu, Phys. Rev. B - Condens. Matter Mater. Phys. 76 (2007).
[56] C. Hin, B.D. Wirth, J. Nucl. Mater. 402 (2010) 30–37.
[57] L. Barnard, N. Cunningham, G.R. Odette, I. Szlufarska, D. Morgan, Acta Mater. 91 (2015) 340–354.
[58] H.J. Frost, K.C. Russell, J. Nucl. Mater. 104 (1981) 1427–1432.
[59] M. Li, M.K. Miller, W.-Y. Chen, J. Nucl. Mater. 462 (2015) 214–220.
[60] L. Tan, T.S. Byun, Y. Katoh, L.L. Snead, Acta Mater. 71 (2014) 11–19.